iScience

CellPress
OPEN ACCESS

Article

EMC3 regulates mesenchymal cell survival via control of the mitotic spindle assembly

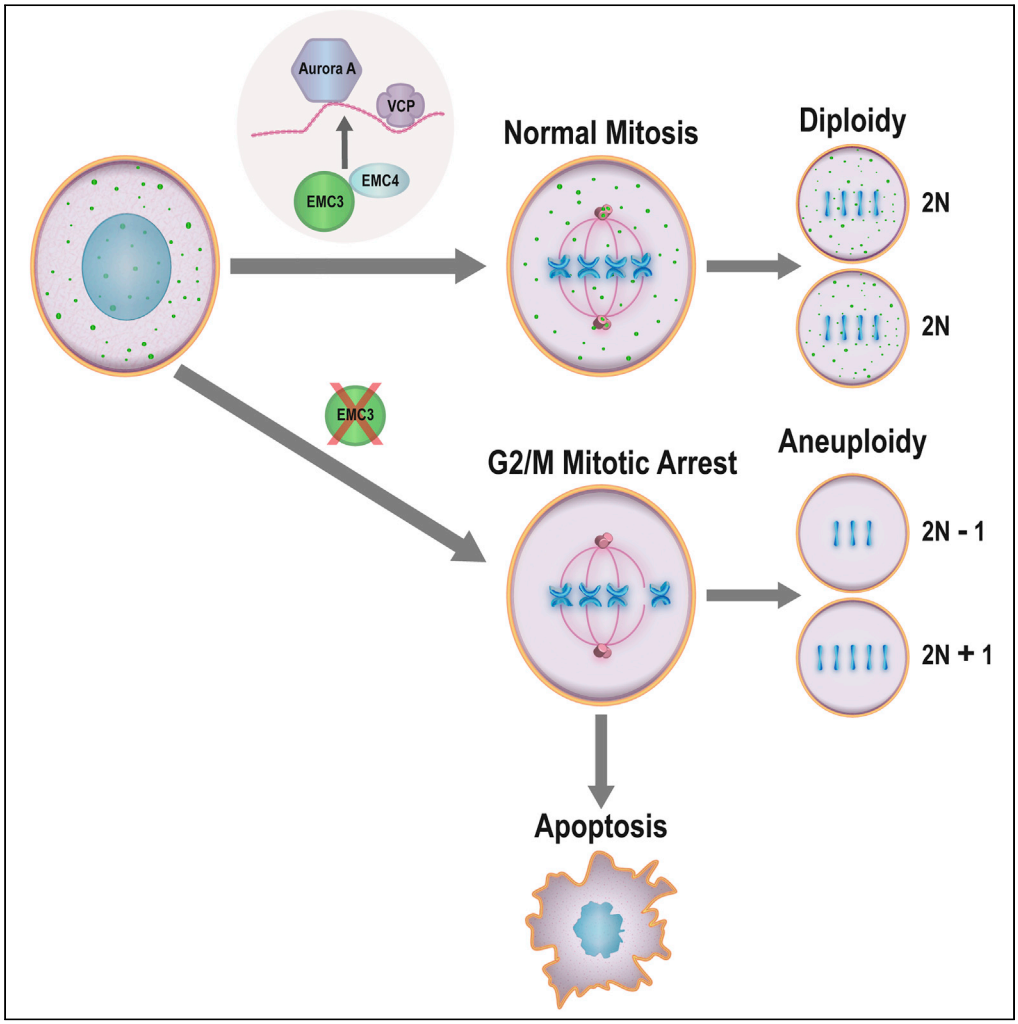

Xiaofang Tang, Wei Wei, John M. Snowball, ..., Charles Ansong, Xinhua Lin, Jeffrey A. Whitsett

xlin@fudan.edu.cn (X.L.)
jeffrey.whitsett@cchmc.org (J.A.W.)

Highlights

EMC3 upregulates protein levels and transits to the centrosomes in mitosis

EMC3 deficiency causes spindle assembly defects, cell cycle arrest, and apoptosis

Multiple EMC3 interactors were identified by mass spectrometry including VCP

EMC3 tightly regulates the levels and activity of Aurora A during mitosis

Tang et al., iScience 26, 105667
January 20, 2023
https://doi.org/10.1016/j.isci.2022.105667

iScience

CellPress
OPEN ACCESS

Article

EMC3 regulates mesenchymal cell survival via control of the mitotic spindle assembly

Xiaofang Tang,[1,2] Wei Wei,[3] John M. Snowball,[1] Ernesto S. Nakayasu,[4] Sheila M. Bell,[1] Charles Ansong,[4] Xinhua Lin,[2,3,*] and Jeffrey A. Whitsett[1,5,*]

SUMMARY

Eukaryotic cells transit through the cell cycle to produce two daughter cells. Dysregulation of the cell cycle leads to cell death or tumorigenesis. Herein, we found a subunit of the ER membrane complex, EMC3, as a key regulator of cell cycle. Conditional deletion of *Emc3* in mouse embryonic mesoderm led to reduced size and patterning defects of multiple organs. *Emc3* deficiency impaired cell proliferation, causing spindle assembly defects, chromosome mis-segregation, cell cycle arrest at G2/M, and apoptosis. Upon entry into mitosis, mesenchymal cells upregulate EMC3 protein levels and localize EMC3 to the mitotic centrosomes. Further analysis indicated that EMC3 works together with VCP to tightly regulate the levels and activity of Aurora A, an essential factor for centrosome function and mitotic spindle assembly: while overexpression of EMC3 or VCP degraded Aurora A, their loss led to increased Aurora A stability but reduced Aurora A phosphorylation in mitosis.

INTRODUCTION

Mitosis is part of the cell cycle which involves a series of steps including prophase, metaphase, anaphase, and telophase, resulting in two daughter nuclei, each carrying a chromosome complement identical to that of the parent nucleus. The mitotic spindle plays a crucial role in the accurate segregation of chromosomes during mitosis, and therefore is paramount for achieving mitotic fidelity and preserving genome integrity. Errors in chromosome segregation during mitosis are linked to cell death as well as tumor initiation and progression.[1–3] The bipolar mitotic spindle is assembled from microtubules, microtubule-associated proteins, and motor proteins in a tightly regulated microtubule nucleation process. In the last three decades, extensive studies on spindle assembly have identified dominant pathways that nucleate microtubules.[4] In most cell types, spindle microtubules are primarily nucleated from two centrosomes, which serve as microtubule-organizing centers and define the spindle poles. However, chromatin- and microtubule-mediated microtubule nucleation pathways can also contribute to mitotic spindle assembly.[4,5] While previous proteomic analyses indicate that approximately 800 proteins and 100 protein complexes may localize on the mitotic spindle[6] and/or contribute to spindle assembly,[7] new spindle assembly factors remain to be discovered. Extensive studies are needed to understand how cells coordinate these factors toward dynamic, precise, and robust spindle assembly leading to mitosis.

ER membrane protein complex (EMC) was first identified in a systematic screening for genes required for protein folding in the ER in *Saccharomyces cerevisiae*.[8] As a ubiquitous and evolutionarily conserved protein complex,[9] EMC has been implicated in a wide range of processes, including ER-associated degradation (ERAD),[10] viral maturation,[11–13] lipid homeostasis,[14,15] organelle communication,[16,17] and biogenesis of multi-pass transmembrane proteins.[14,15,18–21] Biochemical studies of certain EMC client proteins identified the role of EMC in membrane protein biogenesis[22–26]: EMC co-translationally inserts transmembrane domains into lipid bilayers and cooperates with the ER membrane translocon Sec61 to further ensure targeting and accurate topogenesis of membrane proteins.

EMC3, encoded by the mouse *Tmem111* gene, is an essential subunit of EMC. Previously, we generated an *Emc3*^{fl} allele and analyzed the epithelia-specific functions of EMC3 in the lung.[15] Our work demonstrated that in the developing pulmonary epithelium, loss of EMC3 impaired the biogenesis of the phospholipid

[1]Perinatal Institute, Divisions of Neonatology, Perinatal and Pulmonary Biology, Cincinnati Children's Hospital Medical Center, 3333 Burnet Avenue, MLC 7029, Cincinnati, OH 45229, USA

[2]Greater Bay Area Institute of Precision Medicine (Guangzhou), Fudan University, 2nd Nanjiang Rd, Nansha District, Guangzhou 511458, China

[3]State Key Laboratory of Genetic Engineering, School of Life Sciences, Zhongshan Hospital, Fudan University, No. 2005 Songhu Rd, Shanghai 200438, China

[4]Biological Sciences Division, Pacific Northwest National Laboratory, 902 Battelle Blvd, Richland, WA 99354, USA

[5]Lead contact

*Correspondence: xlin@fudan.edu.cn (X.L.), jeffrey.whitsett@cchmc.org (J.A.W.)

https://doi.org/10.1016/j.isci.2022.105667

transport protein ABCA3 as well as the synthesis and packaging of surfactant lipids and proteins, inducing the unfolded protein response (UPR). To further understand the roles of EMC3 in vertebrate development and organ function, we tested whether EMC3 influences organogenesis via control of mesenchymal cell homeostasis. Herein, we show that deletion of *Emc3* in embryonic mesenchymal progenitors caused cell cycle arrest at G2/M and apoptosis without UPR induction, thereby disrupting organ growth and formation. Our data indicate that EMC3 and other components of the EMC complex traffic to centrosomes during mitosis and regulate spindle assembly and cell cycle progression. Our studies not only shed light on the function of the conserved EMC complex and its roles in diverse cellular processes but also provide potential therapeutic targets for cancers and other diseases.

RESULTS

Emc3 deficiency caused cell cycle arrest and apoptosis in fetal pulmonary mesenchyme

To assess potential role(s) of EMC3 in mesenchymal development, the $Emc3^{fl/fl}$ mice were mated to *Dermo1-Cre* (*Twist2-Cre*) transgenic mice[27] which targets mesoderm-derived cells including the skeletal muscle lineages prior to birth. While $Emc3^{fl/fl}$ (referred to as control hereafter) and $Dermo1^{Cre/+}$; $Emc3^{fl/+}$ (referred to as *Emc3 heterozygote* hereafter) mice survived normally without any observable malformations, $Dermo1^{Cre/+}$; $Emc3^{fl/fl}$ (referred to as *Emc3 cKO* hereafter) died of respiratory failure immediately after birth (Table S1). Multiple skeletal defects were observed in the *Emc3 cKO* embryos at E18.5 (Figure S1) indicating an important function of EMC3 in mesodermal development. Omphalocele, resulting from lack of abdominal tissue closure, was found in half of the mutant embryos. All *Emc3*-deficient embryos exhibited abnormal ossification of bones of the face and skull, structural defects of the vertebrae, and shortened/malformed long bones on the hindlimbs. During embryogenesis, *Dermo1-Cre* also directs recombination in developing lung mesenchyme.[28] Loss of *Emc3* caused severe lung malformations during embryonic development. At E18.5, *Emc3 cKO* lungs were markedly reduced in size (Figure 1A) and lung sacculation was impaired (Figure 1D). Multiple cystic lesions were present under the pleural surfaces of the lung (Figure 1A). Consistent with previous findings,[15] *Emc3* deletion reduced protein levels of other EMC subunits, including EMC4 (Figure 1G). We therefore utilized EMC4 staining to trace *Emc3* deletion. The loss of EMC3 signals in the mesenchyme at E16.5 was partially recovered at E18.5 (Figures 1E and 1F). We previously demonstrated widespread but incomplete targeting of pulmonary mesenchyme by *Dermo1-Cre*;[28] the recovery of EMC3 staining later in development is likely related to ongoing proliferation and survival of non-targeted mesenchymal cells. To explore the function of EMC3 in the maintenance of pulmonary mesenchymal cells, we first tested whether EMC3 influenced cell proliferation and/or death. Since *Emc3 cKO* lungs were smaller than control lungs at E16.5 and no significant differences were seen at E15.5 (Figures 1B and 1C), we chose E16.5 for subsequent analyses.

To examine cell proliferation, we stained lung tissues with phospho-histone H3 (pHH3), which is generally used as a marker to label cells at G2 phase and early mitosis. Epithelial cells were stained with FOXA2. The ratio of pHH3+ cells in lung mesenchyme (FOXA2-) from control and *Emc3 cKO* lungs is shown (Figures 2A and 2E). No significant differences were detected between two genotypes. Given the incomplete targeting by *Dermo1-Cre*, we further characterized the mesenchymal subpopulations within *Emc3 cKO* lungs using EMC4 staining to identify *Emc3*-deficient cells. Surprisingly, *Emc3*-deficient (EMC4-, FOXA2-) non-epithelial cells had a higher ratio of pHH3-positive cells compared to *Emc3*-sufficient (EMC4+, FOXA2-) cells (Figures 2A and 2E). To further analyze cell proliferation, bromodeoxyuridine (BrdU) incorporation was assessed following a single pulse of BrdU to more selectively quantify cells at the S phase of the cell cycle. Compared to controls, the entire mesenchymal cell population and the *Emc3*-deficient subpopulation of the *Emc3 cKO* lungs showed significantly decreased numbers of BrdU + cells (Figures 2B and 2F). Differences in the two cell proliferation assays support the concept that *Emc3* deletion dysregulates mitosis and causes G2/M arrest, rather than causing a general inhibition of cell proliferation. Since mitotic arrest can induce cell death,[29,30] we stained the control and *Emc3 cKO* lungs by TUNEL assay (Figure 2C) and for active caspase3 (Figure 2D). Both assays demonstrated increased cell death in pulmonary mesenchymal cells caused by *Emc3* depletion (Figure 2G).

EMC3 has been implicated in UPR, which comprises three parallel sensing pathways, IRE1α/XBP1, ATF6, and PERK/eIF2α. Deletion of *Emc3* in respiratory epithelial cells in the embryonic mouse lung induced the UPR through IRE1α/XBP1 and PERK/eIF2α pathways, as indicated by increased splicing of *Xbp1* mRNA and elevated expression of ATF4 and GADD34, respectively.[15] By contrast, several lines of evidence suggested that UPR was not activated in *Emc3*-deficient mesenchymal cells and therefore did not contribute to the mitotic defects shown before. First, ATF4 and ATF6 antibody staining showed similar signal strength and staining patterns in the control and *Emc3 cKO* lungs (Figures S2A and S2B). Second, we generated primary mouse embryonic fibroblast

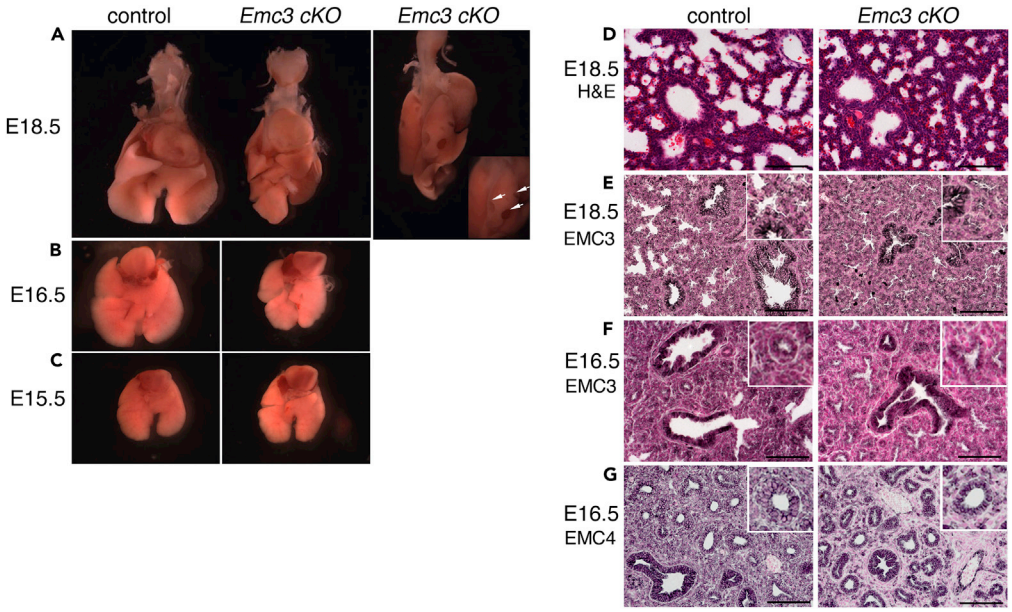

Figure 1. Lung defects with conditional deletion of *Emc3* by *Dermo1-Cre*

(A–C) Lungs from control and *Emc3 cKO* littermates at different embryonic (E) stages are shown. Note that the *Emc3 cKO* lungs were significantly smaller at E16.5 but were similar in size compared to controls at E15.5. Multiple cysts were visible in *Emc3 cKO* lungs at E18.5, possibly related to the death of mesenchymal cells. Inset shows an enlargement of cysts (indicated by arrows) on E18.5 mutant lung.

(D) H&E staining of E18.5 control and *Emc3 cKO* lung sections. Compared to the control, *Emc3 cKO* lungs were developmentally delayed, showing an early stage of sacculation.

(E) EMC3 antibody staining of E18.5 control and *Emc3 cKO* lung sections demonstrates widespread expression of EMC3 in epithelial and mesenchymal cells in control and *Emc3 cKO* lungs.

(F) EMC3 antibody staining of E16.5 control and *Emc3 cKO* lung sections. EMC3 staining was decreased in lung mesenchyme.

(G) EMC4 antibody staining of E16.5 control and *Emc3 cKO* lung sections. *Emc3* deletion decreased EMC4 staining in mesenchyme while staining persisted in respiratory epithelial cells. Scale bars, 100 μm.

(MEF) cells from control, *Emc3 heterozygote*, and *Emc3 cKO* littermates and tested for UPR induction. *Emc3 cKO* MEFs at passage one had comparable protein levels of GADD34 and the master UPR regulator BiP (Figure S2C). *Xbp1* mRNA splicing was not induced in *Emc3 cKO* MEFs (Figure S2D). Third, we examined UPR activity in the fibroblast cell line NIH3T3 following siRNA-mediated knockdown of *Emc3*. *Emc3* siRNA substantially decreased EMC3 as well as EMC4 protein levels (Figures S3A and S3B). In agreement with the mitotic arrest observed *in vivo*, *Emc3* knockdown caused an increased ratio of NIH3T3 cells at G2/M phase (Figure S3C); however, neither ATF4 nor GADD34 levels were altered by *Emc3* siRNA (Figure S3A). Taken together, these data supported the concept that EMC3 regulated cell cycle progression by a process independent of UPR. *Emc4* siRNA treatment caused a similar G2/M arrest (Figure S3C), indicating that EMC3 likely exerts its mitotic functions through EMC.

Mitotic defects and apoptosis in *Emc3*-depleted cells

To further identify mechanisms by which EMC3 regulates mitosis, we examined the MEF cells generated from control, *Emc3 heterozygote*, and *Emc3 cKO* littermates. During passaging, *Emc3*-deficient populations of MEF cells generated from *Emc3 cKO* embryo were rapidly lost, resulting in $Emc3^{+/+}$ cells dominating the previously mixed starting cultures (Figures 3A–3C). By passage 5, *Emc3* mRNA levels in *Emc3 cKO* MEF cultures were almost fully restored to control levels, indicating loss of *Emc3*-deleted cells and survival and expansion of *Emc3*-sufficient cells (Figure 3C). At passage 4, when *Emc3*-deleted cell population was a minority of the *Emc3 cKO* MEF cells in culture, fluorescence-activated cell sorting for the DNA content demonstrated a significant decrease of cells in G2/M phase (Figures 3D and 3E). Consistent with these findings, a "subG" population (cells with fragmented DNA, <2N) was increased in *Emc3 cKO* MEFs, suggesting cell death (Figures 3D and 3E). Increased apoptosis was demonstrated in *Emc3 cKO MEFs* by flow cytometry using annexin V staining (Figure 3F). Notably, an extra peak of propidium iodide staining within G0/G1 was only observed with *Emc3 cKO* MEFs (Figures 3D and 3G). We considered that these

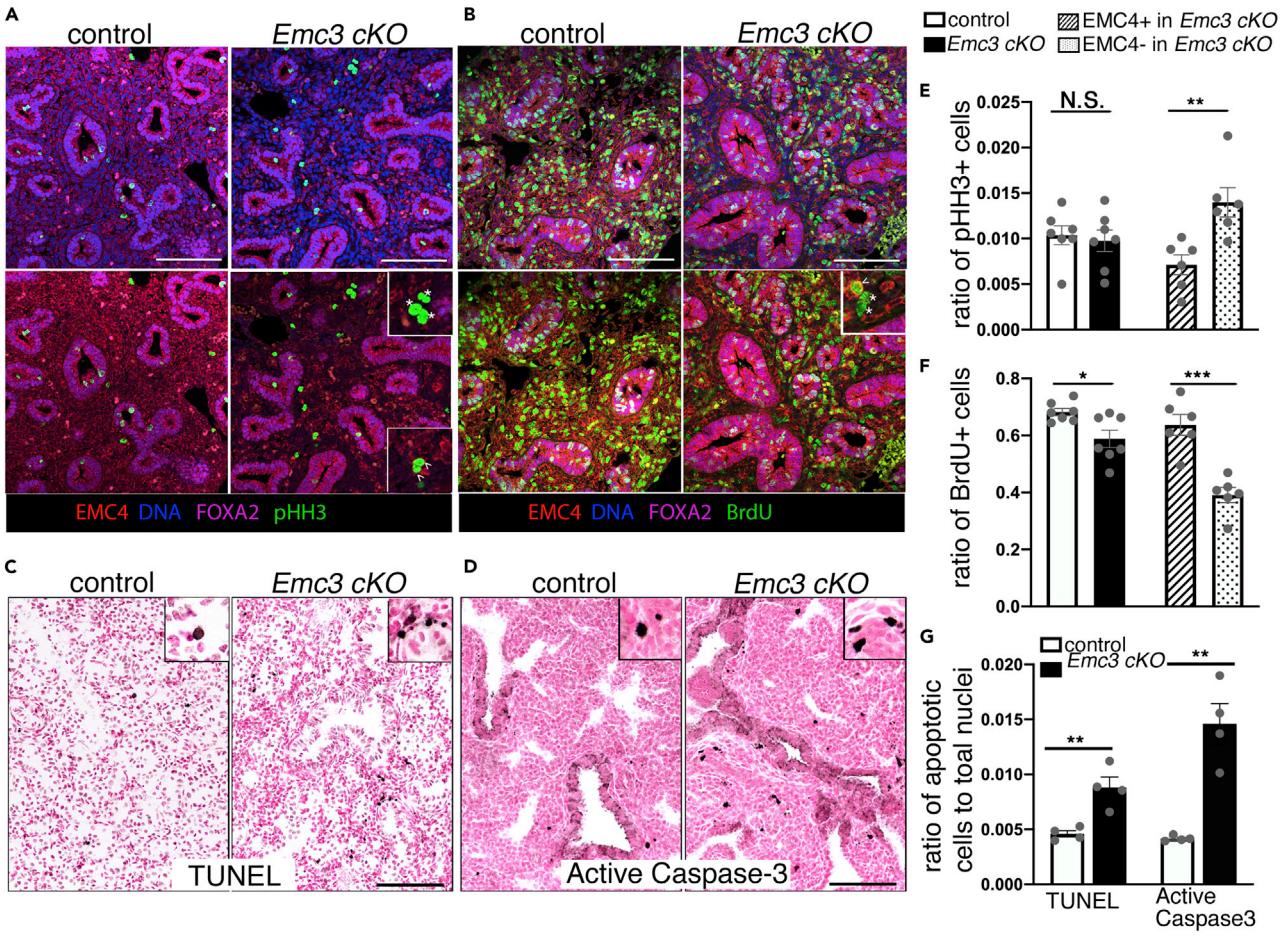

Figure 2. Deletion of *Emc3* in lung mesenchyme causes cell cycle arrest at G2/M phase and cell death

(A and B) Lung sections from E16.5 control and *Emc3*-cKO embryos were stained with antibodies against EMC4, FOXA2, and phospho-histone H3 (pHH3) (A) or with antibodies against EMC4, FOXA2, and BrdU (B). DAPI stained nuclei. EMC4 staining was used to identify sites of *Emc3* deletion. Insets show enlargements of EMC4+ (indicated by >) and EMC4- (indicated by *) cells.

(C and D) TUNEL staining (C) and cleaved caspase-3 antibody staining (D) were used to detect apoptosis on lung sections from E16.5 control and *Emc3*-cKO embryos.

(E and F) Quantification of pHH3 (A) and BrdU (B) staining in control and *Emc3*-cKO lungs. Ratio of pHH3/BrdU positive to total non-epithelial (FOXA2-negative) population in control versus *Emc3*-cKO lungs was quantified. n = 7/group. Within the non-epithelial population of *Emc3*-cKO lungs, ratio of pHH3/BrdU positive to *Emc3*-sufficient (EMC4+) versus *Emc3*-deficient (EMC4-) sub-populations were quantified. A total of 6 *Emc3*-cKO lungs were used for quantification. *Emc3*-deficient mesenchymal cells showed reduced ratio in S phase and increased ratio in G2/M phase of the cell cycle.

(G) The ratio of apoptotic to total nuclei was determined by TUNEL (C) or cleaved caspase-3 staining (D) at E16.5 in control and *Emc3*-cKO lungs, n = 4/group. Ratio of apoptotic to total nuclei was increased in *Emc3*-cKO embryos. Scale bars: 100 μm. Mean ± SEM; *p < 0.05, **p < 0.01, ***p < 0.001 using unpaired, two-tailed Student's t-test.

abnormal cells may represent an aneuploid population caused by chromosome mis-segregation. Alternatively, these cells may enter apoptosis during the G2/M phase of the cell cycle. Both possibilities indicate dysregulation of mitosis after deletion of *Emc3*.

To ensure adequate numbers of *Emc3* mutant cells for analysis, subsequent experiments were performed with MEF cells at passage 2. To label and trace *Emc3*-deficient cells for imaging, we utilized a Cre-inducible transgenic reporter allele, *CAG-CAT-EGFP*.[31] This reporter was used instead of a reporter inserted into the *Rosa26* locus because the *Rosa26* gene is located on the same chromosome as *Emc3*. EGFP expression labeled cells that have undergone Cre-mediated *Emc3* deletion, with decreased EMC3 and EMC4 protein levels detected (Figures S4A–S4E). At passage 3, approximately 70% of the MEF cells generated from *Emc3 heterozygote* embryos were EGFP positive, compared to 30% positive in *Emc3 cKO* MEFs (Figure S4F). These data are consistent with the incomplete targeting by *Dermo1-Cre* as well as the mitotic defects

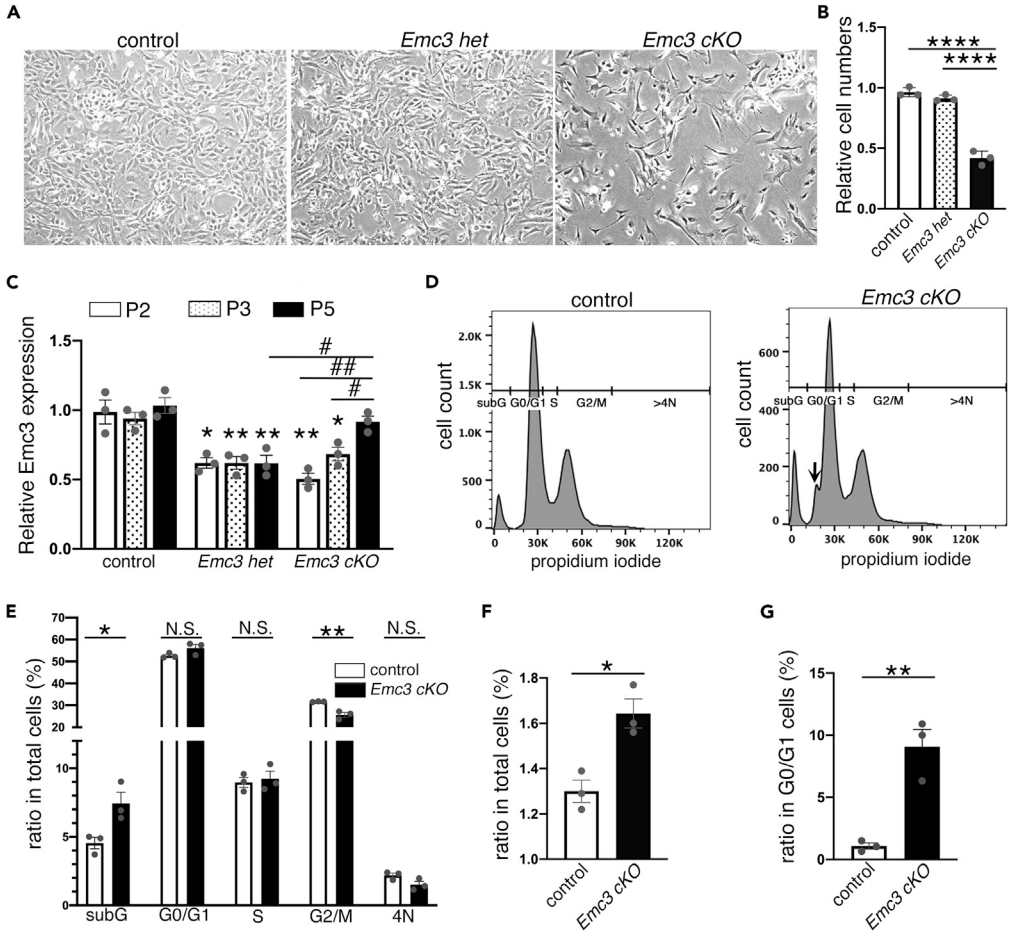

Figure 3. Chromosome segregation defects and cell death in *Emc3*-deleted MEF cells

(A) Equal numbers of MEF cells at passage 1 from control, *Emc3 heterozygote* (*Emc3 het*), and *Emc3 cKO* embryos were plated and cultured in parallel for three days. Representative images of the cells after 3 days of culture are shown.

(B) Statistical analysis of relative cell numbers after 3 days in culture (A). Three independent experiments with MEFs isolated from different embryos were performed. Numbers of *Emc3 cKO* MEFs decreased dramatically after culture. Means ± SEM; One-way ANOVA analysis, $p < 0.0001$. Tukey's post-hoc analysis, ****$p < 0.0001$.

(C) RNAs were extracted from MEF cells at passage 2, 3, and 5 from control, *Emc3 het*, and *Emc3 cKO* embryos (three for each genotype). Relative *Emc3* mRNA levels were quantitated by qPCR. Three independent experiments with MEFs isolated from different embryos were performed. Means ± SEM; One-way ANOVA analysis, $p = 0.0017$. Tukey's post-hoc analysis, *$p < 0.05$, **$p < 0.01$; #$p < 0.05$, ##$p < 0.01$. * indicates statistical analysis of each sample compared to the sample of the same genotype at passage 2. # indicates statistical analysis at passage 5 of *Emc3 cKO* compared to the other two samples.

(D) Control and *Emc3 cKO* MEFs, passage 4, were fixed and stained by propidium iodide and the cell cycle distribution analyzed by flow cytometry. Three independent experiments with MEFs isolated from different embryos were performed. Arrow indicates a peak of subpopulation of cells in G0/G1 with *Emc3 cKO* MEFs.

(E) Statistical analysis of results from (D). Cell cycle distribution of total culture of control and *Emc3 cKO* MEFs was quantified. Significant changes with *Emc3 cKO* MEFs include a decrease of G2/M population and an increase in subG population. Means ± SEM; *$p < 0.05$, **$p < 0.01$ using unpaired, two-tailed Student's t-test.

(F) Apoptosis of control and *Emc3 cKO* MEFs at passage 4 was detected with Annexin V conjugates and analyzed by flow cytometry. Three independent experiments with MEFs isolated from different embryos were performed. Ratio of apoptotic cells was increased in *Emc3 cKO* MEFs. Means ± SEM; *$p < 0.05$ using unpaired, two-tailed Student's t-test.

(G) Statistical analysis of ratio of the subpopulation in G0/G1 (marked by arrow in (D)). A dramatic increase was observed in *Emc3 cKO* MEFs compared to control. Means ± SEM; **$p < 0.01$ using unpaired, two-tailed Student's t-test.

and cell death caused by *Emc3* deletion in the embryos. Using the EGFP reporter, we compared the two subpopulations, $Emc3^{+/+}$ (EGFP negative) and $Emc3^{-/-}$ (EGFP positive) in the *Emc3 cKO* MEFs. Consistent with *in vivo* studies, there was a significant increase in the number of $Emc3^{-/-}$ MEFs arrested in mitosis

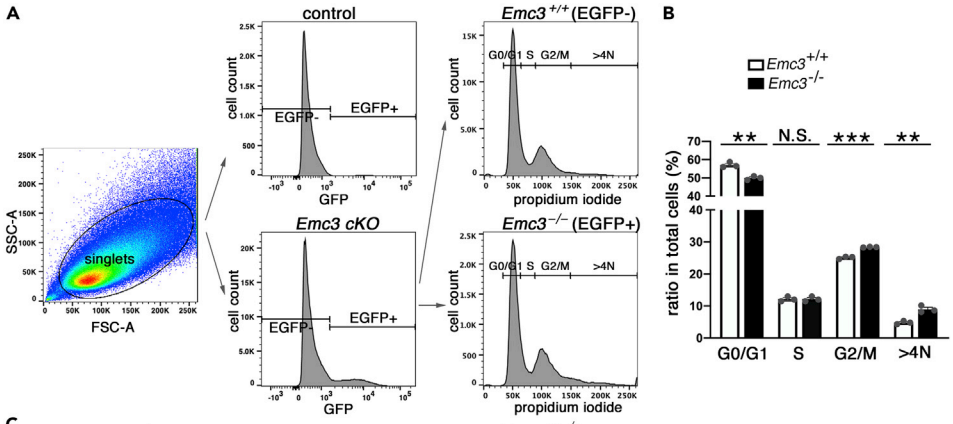
A
control
Emc3 +/+ (EGFP-)
Emc3 cKO
Emc3 −/− (EGFP+)
SSC-A
FSC-A
singlets
EGFP-
EGFP+
cell count
GFP
propidium iodide
G0/G1 S G2/M >4N
B
Emc3+/+
Emc3-/-
ratio in total cells (%)
**
N.S.
***
**
G0/G1
S
G2/M
>4N

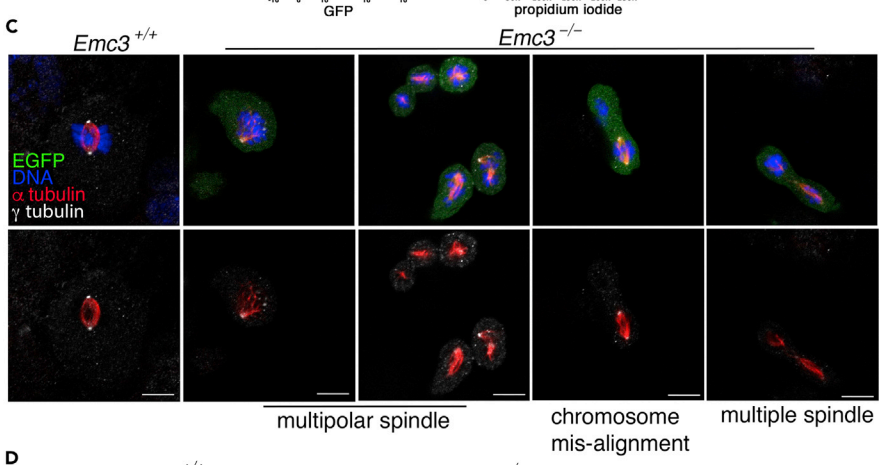
C
Emc3 +/+
Emc3 −/−
EGFP
DNA
α tubulin
γ tubulin
multipolar spindle
chromosome mis-alignment
multiple spindle

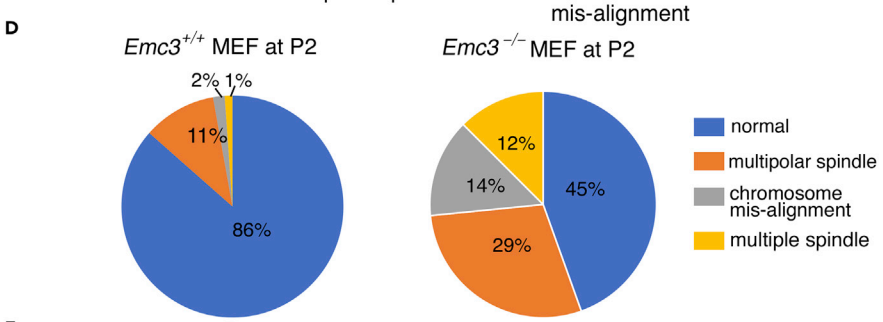
D
Emc3 +/+ MEF at P2
Emc3 −/− MEF at P2
2%
1%
11%
86%
12%
14%
45%
29%
normal
multipolar spindle
chromosome mis-alignment
multiple spindle

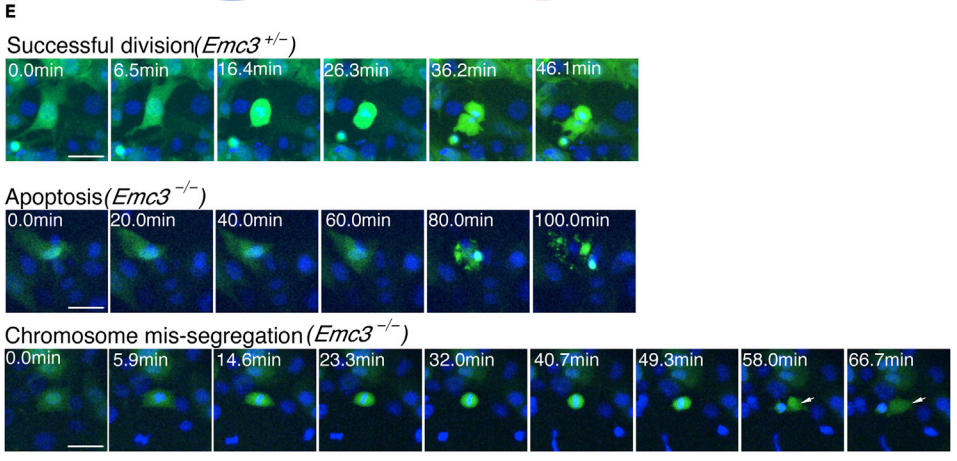
E
Successful division(Emc3 +/−)
0.0min
6.5min
16.4min
26.3min
36.2min
46.1min
Apoptosis(Emc3 −/−)
0.0min
20.0min
40.0min
60.0min
80.0min
100.0min
Chromosome mis-segregation(Emc3 −/−)
0.0min
5.9min
14.6min
23.3min
32.0min
40.7min
49.3min
58.0min
66.7min

Figure 4. Spindle assembly defects and chromosome mis-segregation in *Emc3*-deficient MEF cells

(A) Control and *Emc3 cKO* MEFs carrying Cre-inducible *CAG-CAT-EGFP* allele, passage 2, were fixed and stained by propidium iodide and the cell cycle distribution analyzed by flow cytometry.

(B) Statistic analysis of results from (a). Three independent experiments with MEFs isolated from different embryos were performed. Cell cycle distribution of EGFP-negative (*Emc3* sufficient) and EGFP-positive (*Emc3* deficient) populations of *Emc3 cKO* MEFs was quantified. Means ± SEM; **p < 0.01 ***p < 0.001 using unpaired, two-tailed Student's t-test. The cell cycle distribution of *Emc3*-deficient MEFs demonstrated a significant decrease in G0/G1 and an increase both in G2/M and >4N.

(C) MEF cells, passage 2, from *Emc3-cKO* embryos were stained with antibodies against α tubulin, γ tubulin and DAPI. Cre-induced constitutive expression of an EGFP reporter was used to trace Cre activity and thus to label *Emc3* deletion. Compared to the normal spindle structure of *Emc3*-sufficient cells (EGFP negative, $Emc3^{+/+}$), *Emc3*-deficient cells (EGFP positive, $Emc3^{-/-}$) demonstrated a variety of spindle defects. Scale bars: 10 μm.

(D) Percentage of $Emc3^{+/+}$ or $Emc3^{-/-}$ MEFs stained in (A) with normal or defective spindles. A total of 154 ($Emc3^{+/+}$) and 128 ($Emc3^{-/-}$) MEFs were counted at metaphase. Experiments were repeated three times with MEFs isolated from different embryos. Diverse spindle defects were observed in $Emc3^{-/-}$ MEFs compared to $Emc3^{+/+}$ MEFs.

(E) Images from time-lapse movies of MEF cells were assessed at passage 2 to trace cell cycle progression. Both $Emc3^{+/-}$ (*heterozygote*) and $Emc3^{-/-}$ (mutant) MEFs expressed Cre-induced EGFP reporter. Nuclei were stained with NucBlue Live ReadyProbes (Invitrogen). Cell death during division and uneven chromosomal separation into two daughter cells (note cell without DNA indicated by arrows) were observed in $Emc3^{-/-}$ but not in $Emc3^{+/-}$ MEF cells. Scale bars: 20 μm.

(Figures 4A and 4B). The numbers of $Emc3^{-/-}$ MEF cells with >4N DNA content (Figures 4A and 4B) were also increased, perhaps representing aborted cell division and/or chromosome mis-segregation. Given the crucial role of the mitotic spindle in maintaining mitotic fidelity, we used immunofluorescence staining with alpha tubulin (α tubulin) and gamma tubulin (γ tubulin) to mark spindle microtubules and centrosomes, respectively. Compared to the well-organized bipolar spindle structures in $Emc3^{+/+}$ cells, we observed a significant increase in numbers of $Emc3^{-/-}$ MEFs with various mitotic defects, including multipolar spindles with supernumerary centrosomes, chromosome misalignment, and multiple spindles in individual cells (Figures 4C and 4D). To track individual cells through the cell cycle, we performed time-lapse imaging (Figure 4E) in EGFP-labeled $Emc3^{+/-}$ (generated from *Emc3 heterozygote* embryos) and $Emc3^{-/-}$ MEF cells (EGFP-positive cells in *Emc3 cKO* MEFs). $Emc3^{+/-}$ MEFs underwent mitosis in an average of 60 minutes, resulting in two daughter cells with equal numbers of chromosomes (Figure 4E and Video 1). Mitosis was prolonged (more than 150 min) in some $Emc3^{-/-}$ cells (Video 2), indicating mitotic arrest; some $Emc3^{-/-}$ cells divided into two cells with uneven chromosome segregation, consistent with spindle defects (Figure 4E and Video 3); some $Emc3^{-/-}$ cells underwent apoptosis (Figure 4E and Video 4), consistent with increased cell death detected in the fetal pulmonary mesenchyme *in vivo*. Taken together, the quantitative and dynamic analysis of mitotic defects in *Emc3*-deficient MEF cells supports a role of *Emc3* in spindle assembly and cell cycle progression.

EMC3 locates on the centrosomes and is dynamically regulated during the cell cycle

How does EMC3, an established ER membrane protein, regulate mitotic spindle assembly? To interrogate EMC3 function in mitosis, we first used high-resolution confocal imaging to identify the subcellular localization of EMC3 throughout the cell cycle (Figures 5A and S4C and S4D). During interphase, besides its cytoplasmic distribution in the ER, EMC3 was detected in the nucleus by immunostaining (Figure 5A) and by subcellular fractionation assays (Figure S5). Once cells entered mitosis, EMC3 was detected around centrosomes and mitotic spindle poles in punctate structures (Figure 5A). Another EMC subunit, EMC4, was also located around the spindle poles in mitosis (Figure S6), supporting the concept that EMC acts as a complex in mitosis. Second, the expression of EMC3 and EMC4 was regulated during the cell cycle, with higher expression levels detected during mitosis (Figures 5B and 5C). Multiple important mitotic regulators, including Aurora A and Aurora B, are tightly regulated at mRNA and/or protein levels, as well as, by their subcellular localization. Therefore, the change of EMC protein levels and their recruitment to mitotic spindles further supports a role of EMC in mitotic regulation.

Emc3 depletion increased Aurora A stability but reduced Aurora A activity

To further understand the cause of the mitotic defects in *Emc3*-deficient MEF cells, we stained the mitotic spindle with a series of antibodies against structural components and regulators related to mitosis, demonstrating the disruption of centrosome biogenesis and spindle structure. Among these, Aurora A expression and function were largely disrupted by *Emc3* deletion. Aurora A is an evolutionarily conserved serine/threonine kinase essential for the onset and progression of mitosis and spindle assembly. Numerous studies have characterized the localization of Aurora A at centrosomes as well as at the mitotic spindle.[32–34] Aurora

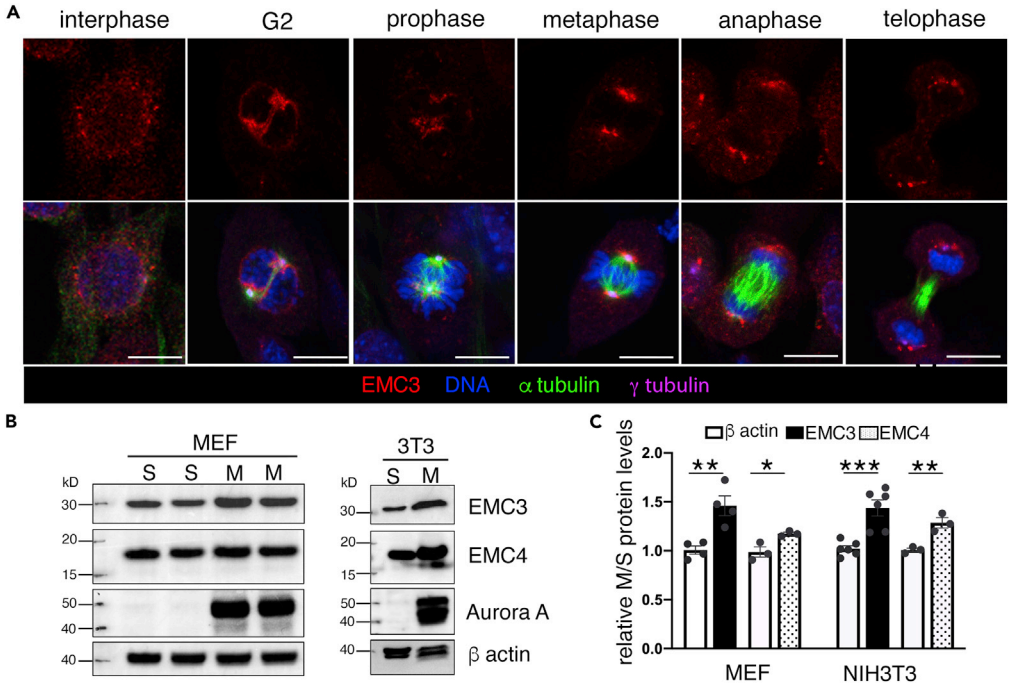

Figure 5. EMC3 traffics to the mitotic centrosomes during mitosis

(A) NIH3T3 cells at different phases of the cell cycle were stained with antibodies against EMC3 (Invitrogen Rabbit Monoclonal Antibody (3H4L5)) and α tubulin. DAPI stained nuclei. EMC3 protein was detected on the mitotic centrosomes during mitosis. Scale bars: 10 μm.

(B) Western blots were performed on whole cell lysates of MEF or NIH3T3 cells synchronized in S phase or M phase. Increased levels of Aurora A were detected in M phase, indicating successful synchronization of S and M phase cells.

(C) Quantification of Western blotting data in (B). Relative protein levels in the whole cell lysates of M phase versus S phase cells were quantified. Both EMC3 (n = 4 for MEF and n = 6 for NIH3T3) and EMC4 (n = 3 for MEF and NIH3T3) levels were significantly increased when MEF/NIH3T3 cells entered mitosis. Mean ± SEM; *p < 0.05, **p < 0.01, ***p < 0.001 using unpaired, two-tailed Student's t-test.

A kinase, once recruited to the centrosome and activated via autophosphorylation,[35,36] promotes centrosome maturation, centrosome integrity, and centrosomal microtubule polymerization. Aurora A is recruited and activated by targeting protein for Xklp2 (TPX2) at the spindle microtubules,[37,38] where it enhances microtubule nucleation mediated by the Ran pathway through cytoplasmic phosphorylation.[39] During mitosis, in comparison to wild-type counterparts, *Emc3*-deficient MEF cells recruited more Aurora A at centrosomes, and further expanded its distribution to the vicinity of centrosomes as well as other cytoplasmic regions (Figure 6A). On the other hand, the activity of Aurora A as indicated by its phosphorylation levels was markedly reduced by *Emc3* deletion (Figure 6B), a finding supported by Western blot analysis of extracts from cell cycle-synchronized mitotic MEF cells (Figures 6C and 6D). To obtain a relatively pure population of *Emc3*-deficient mitotic cells for analysis and to examine the conserved roles of EMC3 in human cells, we treated HeLa cells with control shRNA or *EMC3 shRNA*. As shown in Figure S7, inhibition of *EMC3* caused cell cycle arrest, increased G2/M population, and apoptosis induction, similar to defects in *Emc3* cKO mesenchymal cells. Consistent with the results in MEF cells, knockdown of EMC3 increased total Aurora A protein levels but downregulated the levels of phosphorylated Aurora A (Figures 6E and 6F). These data support a conserved role of EMC3 in the regulation of Aurora A in mitotic eukaryotic cells. Given the important function of Aurora A in spindle formation and cell cycle progression, dysregulation of Aurora A can at least partially account for the mitotic defects caused by *Emc3* depletion.

EMC3 interacts with VCP to control Aurora A degradation and function

To further dissect the mechanism underlying the regulation of EMC3 on Aurora A in mesenchymal cells, we performed affinity mass spectrometry analysis with NIH3T3 cells expressing Myc-tagged EMC3. Proteins and protein groups (n = 23) were identified as potential EMC3 interactors (Figure 7A). Multiple known subunits of the EMC complex, including EMC2/3/5/6/8 (EMC5 is also known as MMGT1), were identified in the

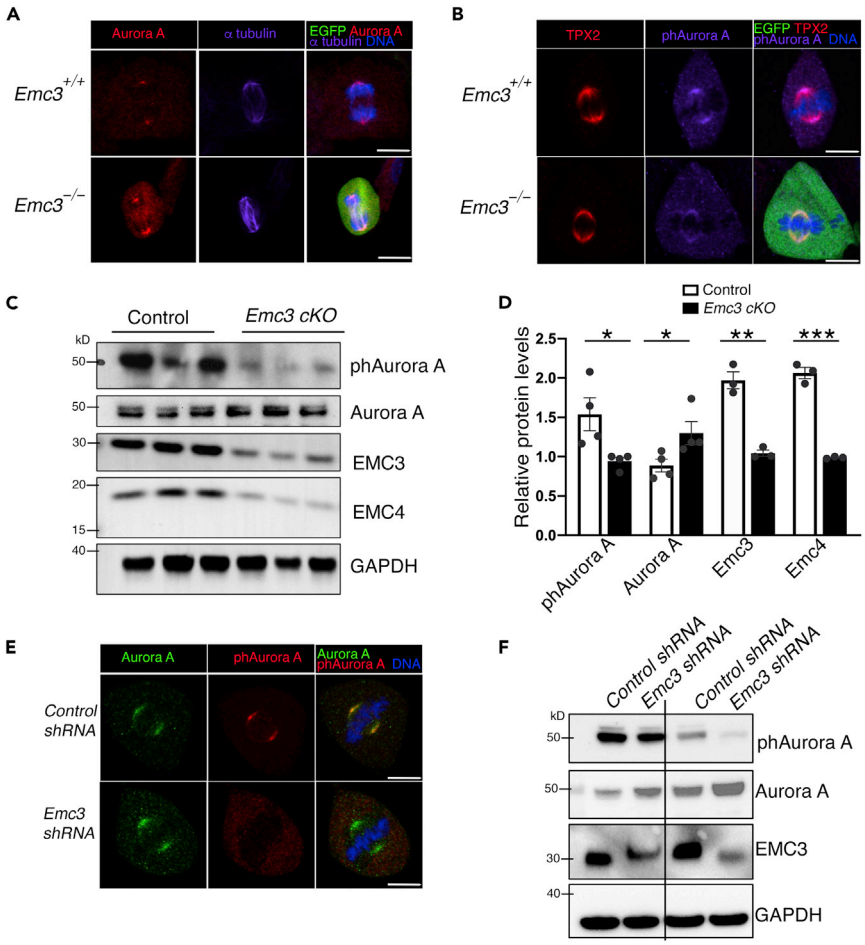

Figure 6. Reduced Aurora A activity by *Emc3* deletion in MEF cells

(A and B) MEF cells, passage 2, from *Emc3-cKO* embryos were stained with antibodies against Aurora A and α tubulin (A) or TPX2 and phosphorylated Aurora A (phAurora A) (B). DAPI stained nuclei. Cre-induced constitutive expression of EGFP was used to label *Emc3* deletion. Compared to *Emc3*-sufficient cells (EGFP negative, $Emc3^{+/+}$), *Emc3*-deficient cells (EGFP positive, $Emc3^{-/-}$) contained more Aurora A but less phAurora A. Scale bars: 10 μm.

(C) MEF cells, passage 2, from control or *Emc3-cKO* embryos were arrested in M phase and harvested for Western blots with indicated antibodies. MEFs isolated from different embryos were analyzed.

(D) Quantification of the relative protein levels in (C). The expression levels of phAurora A (n = 4), Aurora A (n = 4), EMC3 (n = 3), and EMC4 (n = 3) were normalized to that of GAPDH. Mitotic *Emc3-cKO* MEFs expressed less EMC3, EMC4 proteins, and reduced active Aurora A (phosphorylated form) levels. Means ± SEM; *p < 0.05, **p < 0.01, ***p < 0.001 using unpaired, two-tailed Student's t-test.

(E) HeLa cells, infected with control shRNA or Emc3 shRNA, were stained with antibodies against Aurora A and phosphorylated Aurora A (phAurora A). DAPI stained nuclei.

(F) HeLa cells in (E) were arrested in M phase and harvested for Western blots. Representative results are shown from two independent experiments.

immunoprecipitates, supporting the reliability and efficiency of the assay. EMC4 was not identified in this mass spectrometry analysis, likely related to our stringent statistical requirements in the analysis. However, EMC4 was readily identified by Western blots in the immunoprecipitates (Figure S8). Functionally, these proteins represented several cellular processes/pathways (Figure 7B). While EMC3 has been reported in other systems involving ERAD, protein catabolism, and protein folding, novel potential EMC3-interacting proteins were identified (Figures 7A and 7B), including CRYAB, FAF2, BAG2, and valosin containing protein (VCP), further expanding potential roles of EMC3 in protein biogenesis and quality control. While the cell samples were not synchronized to mitotic stages and therefore were not enriched in mitotic factors, several proteins previously discovered as important regulators of mitosis were identified in EMC3 pulldowns. EMC3 co-precipitated CFL1, which is a key regulator of actin cytoskeleton dynamics[40] and is important

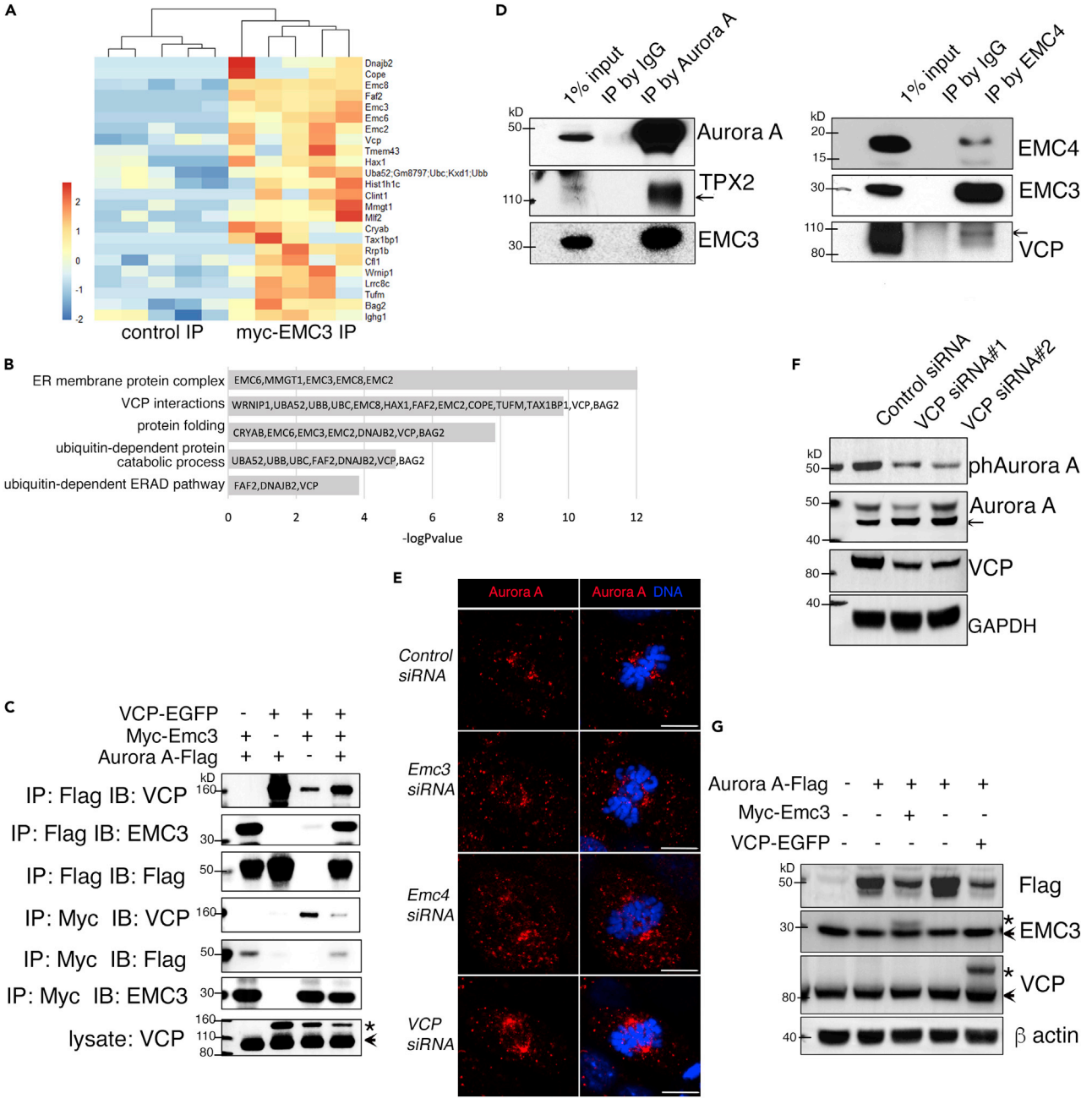

Figure 7. EMC3 interacts with VCP to regulate Aurora A levels and activity

(A) Mass spectrometry of proteins isolated from EMC3 co-immunoprecipitates in NIH3T3 cells identified 23 proteins or protein groups that are potential EMC3 partners. For each experimental pair, NIH3T3 cells were transfected with empty vector (control) or vector encoding Myc-tagged EMC3 (Myc-EMC3). Myc antibody co-immunoprecipitates were isolated from cell lysates using μMACS c-myc Isolation Kit (Miltenyi Biotec) and analyzed by mass spectrometry. Five independent pairs of co-IP assays were performed and analyzed by mass spectrometry. The R package *apmsWAPP* and specifically the sub package TSPM was used to determine significant EMC3-interacting partners, pvalue<.05. Significant EMC3 PPI partners were visualized in a zscore transformed heatmap of the normalized spectral counts.

(B) Functional enrichment analyses of potential EMC3 PPI partners from (A) were performed using Toppgene's Toppfun. A subset of significant relationships was represented by graphing the corresponding -$\log_{10}$(pvalue).

(C) Endogenous EMC4 and Aurora A proteins were immunoprecipitated with anti-EMC4 and anti-Aurora A antibodies, respectively, from HeLa cells. Co-immunoprecipitated proteins were analyzed by Western blots with indicated antibodies.

(D) EMC3 and Aurora A precipitated each other as well as VCP in NIH3T3 cells. Equal numbers of NIH3T3 cells were transfected as indicated. Cell lysates were collected and immunoprecipitated by Flag or Myc antibody. Co-immunoprecipitates were analyzed by Western blots with indicated antibodies.

Figure 7. *Continued*

(E) Mitotic NIH3T3 cells transfected with control siRNA or siRNAs against Emc3, Emc4, or VCP were stained with antibody against Aurora A. DAPI stained nuclei. Note the diffused and enhanced Aurora A expression in Emc3/Emc4/VCP-treated samples. Scale bars: 10 μm.

(F) NIH3T3 cells were transfected with control siRNA or two different *VCP* siRNAs and lysed for Western blots with indicated antibodies. VCP expression was inhibited by the transfection of VCP siRNAs. Higher Aurora A levels and lower phosphorylated Aurora A levels were detected in VCP siRNA samples. *indicates ectopic expression; ←indicates endogenous expression.

(G) Equal numbers of NIH3T3 cells were transfected with Myc-Emc3, Aurora A-Flag, and/or VCP-EGFP cDNAs as indicated. Cell lysates were collected and analyzed by Western blots with indicated antibodies. Ectopic expression of either Myc-Emc3 or VCP-EGFP reduced the stability of Aurora A-Flag. *indicates ectopic expression; ←indicates endogenous expression.

for normal mitotic progression and cytokinesis.[41] Interestingly, half of the EMC3 binding partners were the conserved AAA ATPase VCP (also known as p97/Cdc48)[42] and its interactors. Integral to a wide array of cellular processes, VCP has also been implicated in the control of spindle formation in part through Aurora A function. Consistent with the notion that EMC3 regulates Aurora A via VCP, the three proteins, Flag-tagged Aurora A, EGFP-tagged VCP, and Myc-tagged EMC3, precipitated each other (Figures S9 and 7C). Moreover, the interaction between EMC3, VCP, and Aurora A during mitosis was confirmed in HeLa cells. Co-immunoprecipitation (co-IP) with an Aurora A antibody pulled down endogenous EMC3 as well as an Aurora A cofactor, TPX2 (Figure 7D). While available EMC3 antibodies were not sufficient for co-IP assays, EMC4 antibody precipitated endogenous EMC3 and VCP (Figure 7D). Taken together, the co-IP assays indicate that EMC, VCP, and Aurora A may form a complex during mitosis.

How does VCP regulate Aurora A during mitosis? At the entry of mitosis, VCP coordinates centrosome maturation timing by limiting the centrosomal recruitment of Aurora A.[43] With mitosis progression, VCP is required for disassembly of mitotic spindles by directly binding to and extracting spindle assembly factors including Aurora A and Aurora B from chromatin.[44–47] In agreement with the interaction of EMC3, VCP, and Aurora A in mitosis, EMC3 and VCP exert similar effects on Aurora A stability and function. On one hand, siRNA-mediated knockdown of VCP led to centrosomal and cytoplasmic accumulation of Aurora A with less Aurora A phosphorylation (Figures 7E and 7F), similar to the effects caused by Emc3/Emc4 knockdown (Figures 6E and 6F, and 7E) or Emc3 deletion (Figures 6A–6D). On the other hand, overexpression of either EMC3 or VCP further enhanced Aurora A degradation (Figure 7G), opposite to the effects caused by EMC3/VCP deficiency. As a substrate of the anaphase-promoting complex/cyclosome ubiquitin ligase,[48] Aurora A is tightly regulated by proteasomal degradation (Figure S10A). Overexpression of EMC3 led to reduced Aurora A stability, which was blocked by treatment with proteasome inhibitors MG132 and lactacystin (Figure S10B). Considering the established role of VCP in unfolding ubiquitinated substrates to render it accessible for degradation[49] and that of EMC3 in targeting unfolded proteins for proteasome degradation, it is reasonable to speculate the cooperative action of EMC3 and VCP during mitosis: EMC3 works together with VCP to spatiotemporally regulate Aurora A activity to ensure robust Aurora A activation at the entry of mitosis and removal of Aurora A from the cells with mitotic progression.

DISCUSSION

Recent studies on EMC3 and the EMC complex have been focused on their roles in membrane protein biogenesis and membrane insertion in the ER. Data presented herein identify an unexpected role for EMC3 in control of mitotic spindle assembly and cell cycle progression, mediated at least in part through regulation of Aurora A stability and function. We have shown that in *Emc3*-depleted mesenchymal cells, both centrosome biogenesis and spindle microtubule organization are disrupted, causing mitotic arrest, chromosome mis-segregation, and apoptosis. Our work further extends knowledge regarding the evolutionarily conserved EMC complex by identifying a cell-type-specific function in mesenchymal cells.

Present data demonstrated the subcellular localization of EMC3 and EMC4 in the nucleus and on the mitotic centrosomes. Work from our group and others demonstrated the presence of EMC3 in the ER, mitochondria,[16] as well as, in the lamellar body, a lysosome-derived organelle.[15] Staining of the EMC subunits with specific antibodies by the Cell Atlas[50] indicated that EMC6 is localized to the centrosome and the nucleoplasm and EMC9 localizes to the Golgi apparatus. Thus, the EMC complex is not exclusively ER-resident and traffics into a number of intracellular compartments. In particular, ER is dramatically reorganized in mitosis, forming a tubular network around the centrosomes.[51–53] An ER membrane protein CLIMP63ER was recently found to preferentially interact with centrosome microtubules.[54] Therefore, ER proteins

including EMC3 and EMC4 can potentially associate with centrosomes through microtubules in mitosis. Alternatively, dynamic interaction of EMC subunits may be regulated through interaction with diverse protein partners. VCP, also known as transitional ER ATPase, is a strong EMC3-interacting protein identified by our affinity mass spectrometry. VCP has been found in other organelles and in cytosol and nucleus. Recently, it was demonstrated that VCP is recruited to the centrosome and spindle during mitosis.[55] The dynamic subcellular localization of EMC subunits supports their pleiotropic functions outside of the ER and implies that EMC composition might vary for distinct functions and in diverse cellular contexts.

Present data support the indispensable role of EMC3 in control of the cell cycle in mesenchymal cells. However, it is increasingly clear that EMC subunits and their functions are highly cell selective. In our previous work, epithelia-specific deletion of *Emc3* severely impaired surfactant production; however, *Emc3* mutant pulmonary epithelial progenitor cells proliferated and differentiated normally until birth. While we do observe similar mitotic spindle localization of EMC3 in epithelial cells, it was not required for the mitosis of lung epithelial cells. One possible explanation is that the function of EMC3 in regulating epithelial growth is redundant or the availability of other cofactors is cell type dependent. Alternatively, the underlying mechanisms for spindle assembly and cell cycle regulation may vary among cell types during development. For instance, inhibition of Aurora A by RNA interference or inhibitors has cell-selective effects in cultured mammalian cells. Aurora A RNAi in HeLa cells blocks or delays mitotic entry,[56,57] while in other transformed cell types, Aurora A depletion or inhibition causes mitotic arrest with monopolar spindles,[58,59] daughter cells with spindle abnormalities, and chromosome segregation defects leading to aneuploidy.[60]

Based on the interaction of EMC3 and VCP and their similar roles in the regulation of Aurora A during mitosis, we propose that EMC3 and VCP work together to regulate mitotic spindle assembly. Inhibition of EMC3/EMC4 or VCP generated two seemingly opposing effects on Aurora A: increased total Aurora A levels and decreased Aurora A activity (phosphorylation). While the latter was the primary effect and was consistently detected after EMC3/EMC4 inhibition, the former was only obvious with deletion or strong knockdown of EMC3/EMC4 (Figures S3B and 7E), suggesting two independent mechanisms. How EMC3/EMC4 regulates Aurora A activity needs further study; reduced centrosomal TPX2 and phosphorylated Aurora A levels (Figure 6B) suggest that EMC may impair recruitment of Aurora A to the centrosome and/or its activation by TPX2. Similarly, VCP was shown to control centrosomal recruitment of Aurora A.[43] Increased total Aurora A and a more diffuse distribution pattern were seen after prolonged deficiency of EMC3/VCP, probably related to reduced proteasomal degradation of Aurora A. Both EMC and VCP are involved in ERAD and VCP was demonstrated to regulate ubiquitinated Aurora B during mitosis.[45] Regulation of Aurora A by EMC and VCP on Aurora A may occur after all three are recruited to the mitotic centrosome. While VCP and its cofactors comprised the largest group in EMC3 precipitates, it is likely that EMC3 and VCP coordinate in other cellular contexts and on substrates other than Aurora A, including Aurora B. Future studies are needed to further investigate the interaction of EMC3 and VCP in other cellular processes.

Present findings demonstrated that deficiency in either *Emc3* or *Emc4* caused mitotic abnormalities and Aurora A dysregulation in mesenchymal cells. Dysregulation of Aurora A has been implicated in abnormal centrosomes, defective mitotic spindle formation, and aneuploidy and has been linked to multiple human diseases including cancer.[61–63] Consistent with their essential role in mitosis, dysregulation of EMC may be involved in organogenesis, tissue repair, and tumorigenesis. Genomic sequencing data by The Cancer Genome Atlas (TCGA, https://www.cancer.gov) demonstrate that chromosome number variations and somatic mutations of EMC3 as well as other EMCs are frequently identified in a variety of cancers. Therefore, modulation of EMC levels and/or function may provide new approaches for future therapies.

Limitations of the study

1. We were not able to find useful EMC3 antibody for immunostaining on tissue sections and for co-immunoprecipitation in cell lysates. Since EMC4 had a similar role and subcellular localization during mitosis, we utilized EMC4 antibody.
2. Present and past work suggest the dynamic subcellular localization of EMC3 and other EMC subunits. Due to the scope of this study, the underlying mechanism(s) of its trafficking were not explored, and more work is needed to interrogate this issue.

3. This work focused on the role of EMC3 in mitosis in mesenchymal cells. How EMC3 is involved in mitosis in their cell types and how other EMC subunits are involved in mitosis were not identified and beyond the scope of this study and await further investigation.

STAR★METHODS

Detailed methods are provided in the online version of this paper and include the following:

- KEY RESOURCES TABLE
- RESOURCE AVAILABILITY
  - Lead contact
  - Materials availability
  - Data and code availability
- EXPERIMENTAL MODEL AND SUBJECT DETAILS
  - Mice
  - Cell lines
  - MEF cells
- METHOD DETAILS
  - Alizarin red and alcian blue staining of bone and cartilage
  - Lung histology, immunohistochemistry and immunofluorescence
  - Constructs, siRNAs and shRNAs
  - Cell transfection and western blots
  - Time-lapse imaging
  - Cell synchronization
  - RNA isolation and qPCR
  - Flow cytometry
  - Proteomic analysis
- QUANTIFICATION AND STATISTICAL ANALYSIS
  - Statistical analysis
  - Quantification of cell proliferation and cell death in the lung
  - Quantification of mass spectrometry data

SUPPLEMENTAL INFORMATION

Supplemental information can be found online at https://doi.org/10.1016/j.isci.2022.105667.

ACKNOWLEDGMENTS

We thank the Confocal Imaging Core at Cincinnati Children's Hospital Medical Center for technical assistance on time-lapse imaging and quantification; we thank Mehari Endale and Jerilyn Gray for technical assistance on flow cytometry; we thank Dr. Anna Perl and Dr. Tanya Kalin for discussion on the experimental design; we thank Anusha Sridharan for making the graphic abstract. This work was supported by NIH grants R01HL136722 (to J.A.W. and X.L.) and U01HL134745 (to J.A.W.), and a startup grant (I0018) from the Greater Bay Area Institute of Precision Medicine (Guangzhou) (to X.T.).

AUTHOR CONTRIBUTIONS

X.T. characterized the defects and performed all cell culture experiments. X.T. and W.W. did immuno-histochemistry, immune-fluorescence, and Western blotting studies. E.S.N. and C.A. performed mass spectrometry. J.M.S. analyzed the mass spectrometry data. S.B. did the Alizarin red and blue staining of bone and cartilage. X.T. and J.A.W. designed and interpreted the experiments. X.T., X.L., and J.A.W. wrote the manuscript.

DECLARATION OF INTERESTS

The authors declare no competing interests.

Received: December 29, 2021
Revised: August 15, 2022
Accepted: November 21, 2022
Published: January 20, 2023

REFERENCES

1. Funk, L.C., Zasadil, L.M., and Weaver, B.A. (2016). Living in CIN: mitotic infidelity and its consequences for tumor promotion and suppression. Dev. Cell *39*, 638–652.

2. Lengauer, C., Kinzler, K.W., and Vogelstein, B. (1998). Genetic instabilities in human cancers. Nature *396*, 643–649.

3. Stumpff, J., Ghule, P.N., Shimamura, A., Stein, J.L., and Greenblatt, M. (2014). Spindle microtubule dysfunction and cancer predisposition. J. Cell. Physiol. *229*, 1881–1883.

4. Prosser, S.L., and Pelletier, L. (2017). Mitotic spindle assembly in animal cells: a fine balancing act. Nat. Rev. Mol. Cell Biol. *18*, 187–201.

5. Walczak, C.E., and Heald, R. (2008). Mechanisms of mitotic spindle assembly and function. Int. Rev. Cytol. *265*, 111–158.

6. Sauer, G., Körner, R., Hanisch, A., Ries, A., Nigg, E.A., and Silljé, H.H.W. (2005). Proteome analysis of the human mitotic spindle. Mol. Cell. Proteomics *4*, 35–43.

7. Hutchins, J.R.A., Toyoda, Y., Hegemann, B., Poser, I., Hériché, J.K., Sykora, M.M., Augsburg, M., Hudecz, O., Buschhorn, B.A., Bulkescher, J., et al. (2010). Systematic analysis of human protein complexes identifies chromosome segregation proteins. Science *328*, 593–599.

8. Jonikas, M.C., Collins, S.R., Denic, V., Oh, E., Quan, E.M., Schmid, V., Weibezahn, J., Schwappach, B., Walter, P., Weissman, J.S., and Schuldiner, M. (2009). Comprehensive characterization of genes required for protein folding in the endoplasmic reticulum. Science *323*, 1693–1697.

9. Wideman, J.G. (2015). The ubiquitous and ancient ER membrane protein complex (EMC): tether or not? F1000Res. *4*, 624.

10. Christianson, J.C., Olzmann, J.A., Shaler, T.A., Sowa, M.E., Bennett, E.J., Richter, C.M., Tyler, R.E., Greenblatt, E.J., Harper, J.W., and Kopito, R.R. (2011). Defining human ERAD networks through an integrative mapping strategy. Nat. Cell Biol. *14*, 93–105.

11. Rothan, H.A., and Kumar, M. (2019). Role of endoplasmic reticulum-associated proteins in flavivirus replication and assembly complexes. Pathogens *8*, 148.

12. Lin, D.L., Inoue, T., Chen, Y.J., Chang, A., Tsai, B., and Tai, A.W. (2019). The ER membrane protein complex promotes biogenesis of dengue and zika virus non-structural multi-pass transmembrane proteins to support infection. Cell Rep. *27*, 1666–1674.e4.

13. Bagchi, P., Inoue, T., and Tsai, B. (2016). EMC1-dependent stabilization drives membrane penetration of a partially destabilized non-enveloped virus. Elife *5*, e21470.

14. Volkmar, N., Thezenas, M.L., Louie, S.M., Juszkiewicz, S., Nomura, D.K., Hegde, R.S., Kessler, B.M., and Christianson, J.C. (2019). The ER membrane protein complex promotes biogenesis of sterol-related enzymes maintaining cholesterol homeostasis. J. Cell Sci. *132*, jcs223453.

15. Tang, X., Snowball, J.M., Xu, Y., Na, C.L., Weaver, T.E., Clair, G., Kyle, J.E., Zink, E.M., Ansong, C., Wei, W., et al. (2017). EMC3 coordinates surfactant protein and lipid homeostasis required for respiration. J. Clin. Invest. *127*, 4314–4325.

16. Lahiri, S., Chao, J.T., Tavassoli, S., Wong, A.K.O., Choudhary, V., Young, B.P., Loewen, C.J.R., and Prinz, W.A. (2014). A conserved endoplasmic reticulum membrane protein complex (EMC) facilitates phospholipid transfer from the ER to mitochondria. PLoS Biol. *12*, e1001969.

17. Bagchi, P., Torres, M., Qi, L., and Tsai, B. (2020). Selective EMC subunits act as molecular tethers of intracellular organelles exploited during viral entry. Nat. Commun. *11*, 1127.

18. Xiong, L., Zhang, L., Yan, Y., Li, N., Lai, W., Wang, F., Zhu, X., Wang, Y., et al. (2020). ER complex proteins are required for rhodopsin biosynthesis and photoreceptor survival in Drosophila and mice. Cell Death Differ. *27*, 646–661.

19. Satoh, T., Ohba, A., Liu, Z., Inagaki, T., and Satoh, A.K. (2015). dPob/EMC is essential for biosynthesis of rhodopsin and other multi-pass membrane proteins in Drosophila photoreceptors. Elife *4*, e06306.

20. Taylor, M.R., Kikkawa, S., Diez-Juan, A., Ramamurthy, V., Kawakami, K., Carmeliet, P., and Brockerhoff, S.E. (2005). The zebrafish pob gene encodes a novel protein required for survival of red cone photoreceptor cells. Genetics *170*, 263–273.

21. O'Donnell, J.P., Phillips, B.P., Yagita, Y., Juszkiewicz, S., Wagner, A., Malinverni, D., Keenan, R.J., Miller, E.A., and Hegde, R.S. (2020). The architecture of EMC reveals a path for membrane protein insertion. Elife *9*, e57887.

22. Hiramatsu, N., Tago, T., Satoh, T., and Satoh, A.K. (2019). ER membrane protein complex is required for the insertions of late-synthesized transmembrane helices of Rh1 in Drosophila photoreceptors. Mol. Biol. Cell *30*, 2890–2900.

23. Chitwood, P.J., and Hegde, R.S. (2019). The role of EMC during membrane protein biogenesis. Trends Cell Biol. *29*, 371–384.

24. Shurtleff, M.J., Itzhak, D.N., Hussmann, J.A., Schirle Oakdale, N.T., Costa, E.A., Jonikas, M., Weibezahn, J., Popova, K.D., Jan, C.H., Sinitcyn, P., Vembar, S.S., et al. (2018). The ER membrane protein complex interacts cotranslationally to enable biogenesis of multipass membrane proteins. Elife *7*, e37018.

25. Chitwood, P.J., Juszkiewicz, S., Guna, A., Shao, S., and Hegde, R.S. (2018). EMC is required to initiate accurate membrane protein topogenesis. Cell *175*, 1507–1519.e16.

26. Coelho, J.P.L., Stahl, M., Bloemeke, N., Meighen-Berger, K., Alvira, C.P., Zhang, Z.R., Sieber, S.A., and Feige, M.J. (2019). A network of chaperones prevents and detects failures in membrane protein lipid bilayer integration. Nat. Commun. *10*, 1908.

27. Yu, K., Xu, J., Liu, Z., Sosic, D., Shao, J., Olson, E.N., Towler, D.A., and Ornitz, D.M. (2003). Conditional inactivation of FGF receptor 2 reveals an essential role for FGF signaling in the regulation of osteoblast function and bone growth. Development *130*, 3063–3074.

28. Lange, A.W., Haitchi, H.M., LeCras, T.D., Sridharan, A., Xu, Y., Wert, S.E., James, J., Udell, N., Thurner, P.J., and Whitsett, J.A. (2014). Sox17 is required for normal pulmonary vascular morphogenesis. Dev. Biol. *387*, 109–120.

29. Matson, D.R., and Stukenberg, P.T. (2011). Spindle poisons and cell fate: a tale of two pathways. Mol. Interv. *11*, 141–150.

30. Vitale, I., Galluzzi, L., Castedo, M., and Kroemer, G. (2011). Mitotic catastrophe: a mechanism for avoiding genomic instability. Nat. Rev. Mol. Cell Biol. *12*, 385–392.

31. Nakamura, T., Colbert, M.C., and Robbins, J. (2006). Neural crest cells retain multipotential characteristics in the developing valves and label the cardiac conduction system. Circ. Res. *98*, 1547–1554.

32. Barr, A.R., and Gergely, F. (2007). Aurora-A: the maker and breaker of spindle poles. J. Cell Sci. *120* (Pt 17), 2987–2996.

33. Giet, R., McLean, D., Descamps, S., Lee, M.J., Raff, J.W., Prigent, C., and Glover, D.M. (2002). Drosophila Aurora A kinase is required to localize D-TACC to centrosomes and to regulate astral microtubules. J. Cell Biol. *156*, 437–451.

34. Roghi, C., Giet, R., Uzbekov, R., Morin, N., Chartrain, I., Le Guellec, R., Couturier, A., Dorée, M., Philippe, M., and Prigent, C. (1998). The Xenopus protein kinase pEg2 associates with the centrosome in a cell cycle-dependent manner, binds to the spindle microtubules and is involved in bipolar mitotic spindle assembly. J. Cell Sci. *111* (Pt 5), 557–572.

35. Reboutier, D., Troadec, M.B., Cremet, J.Y., Fukasawa, K., and Prigent, C. (2012). Nucleophosmin/B23 activates Aurora A at the centrosome through phosphorylation of serine 89. J. Cell Biol. *197*, 19–26.

36. Joukov, V., De Nicolo, A., Rodriguez, A., Walter, J.C., and Livingston, D.M. (2010). Centrosomal protein of 192 kDa (Cep192) promotes centrosome-driven spindle assembly by engaging in organelle-specific Aurora A activation. Proc. Natl. Acad. Sci. USA *107*, 21022–21027.

37. Zorba, A., Buosi, V., Kutter, S., Kern, N., Pontiggia, F., Cho, Y.J., and Kern, D. (2014). Molecular mechanism of Aurora A kinase

autophosphorylation and its allosteric activation by TPX2. Elife *3*, e02667.

38. Gruss, O.J., and Vernos, I. (2004). The mechanism of spindle assembly: functions of Ran and its target TPX2. J. Cell Biol. *166*, 949–955.

39. Sardon, T., Peset, I., Petrova, B., and Vernos, I. (2008). Dissecting the role of Aurora A during spindle assembly. EMBO J. *27*, 2567–2579.

40. Vartiainen, M.K., Mustonen, T., Mattila, P.K., Ojala, P.J., Thesleff, I., Partanen, J., and Lappalainen, P. (2002). The three mouse actin-depolymerizing factor/cofilins evolved to fulfill cell-type-specific requirements for actin dynamics. Mol. Biol. Cell *13*, 183–194.

41. Amano, T., Kaji, N., Ohashi, K., and Mizuno, K. (2002). Mitosis-specific activation of LIM motif-containing protein kinase and roles of cofilin phosphorylation and dephosphorylation in mitosis. J. Biol. Chem. *277*, 22093–22102.

42. Bodnar, N., and Rapoport, T. (2017). Toward an understanding of the Cdc48/p97 ATPase. F1000Res. *6*, 1318.

43. Kress, E., Schwager, F., Holtackers, R., Seiler, J., Prodon, F., Zanin, E., Eiteneuer, A., Toya, M., Sugimoto, A., Meyer, H., et al. (2013). The UBXN-2/p37/p47 adaptors of CDC-48/p97 regulate mitosis by limiting the centrosomal recruitment of Aurora A. J. Cell Biol. *201*, 559–575.

44. Cao, K., Nakajima, R., Meyer, H.H., and Zheng, Y. (2003). The AAA-ATPase Cdc48/p97 regulates spindle disassembly at the end of mitosis. Cell *115*, 355–367.

45. Ramadan, K., Bruderer, R., Spiga, F.M., Popp, O., Baur, T., Gotta, M., and Meyer, H.H. (2007). Cdc48/p97 promotes reformation of the nucleus by extracting the kinase Aurora B from chromatin. Nature *450*, 1258–1262.

46. Heallen, T.R., Adams, H.P., Furuta, T., Verbrugghe, K.J., and Schumacher, J.M. (2008). An Afg2/Spaf-related Cdc48-like AAA ATPase regulates the stability and activity of the C. elegans Aurora B kinase AIR-2. Dev. Cell *15*, 603–616.

47. Dobrynin, G., Popp, O., Romer, T., Bremer, S., Schmitz, M.H.A., Gerlich, D.W., and Meyer, H. (2011). Cdc48/p97-Ufd1-Npl4 antagonizes Aurora B during chromosome segregation in HeLa cells. J. Cell Sci. *124* (Pt 9), 1571–1580.

48. Floyd, S., Pines, J., and Lindon, C. (2008). APC/C Cdh1 targets aurora kinase to control reorganization of the mitotic spindle at anaphase. Curr. Biol. *18*, 1649–1658.

49. Beskow, A., Grimberg, K.B., Bott, L.C., Salomons, F.A., Dantuma, N.P., and Young, P. (2009). A conserved unfoldase activity for the p97 AAA-ATPase in proteasomal degradation. J. Mol. Biol. *394*, 732–746.

50. Thul, P.J., Åkesson, L., Wiking, M., Mahdessian, D., Geladaki, A., Ait Blal, H., Alm, T., Asplund, A., Björk, L., Breckels, L.M., et al. (2017). A subcellular map of the human proteome. Science *356*, eaal3321.

51. Karabasheva, D., and Smyth, J.T. (2019). A novel, dynein-independent mechanism focuses the endoplasmic reticulum around spindle poles in dividing Drosophila spermatocytes. Sci. Rep. *9*, 12456.

52. Puhka, M., Joensuu, M., Vihinen, H., Belevich, I., and Jokitalo, E. (2012). Progressive sheet-to-tubule transformation is a general mechanism for endoplasmic reticulum partitioning in dividing mammalian cells. Mol. Biol. Cell *23*, 2424–2432.

53. Puhka, M., Vihinen, H., Joensuu, M., and Jokitalo, E. (2007). Endoplasmic reticulum remains continuous and undergoes sheet-to-tubule transformation during cell division in mammalian cells. J. Cell Biol. *179*, 895–909.

54. Zheng, P., Obara, C.J., Szczesna, E., Nixon-Abell, J., Mahalingan, K.K., Roll-Mecak, A., Lippincott-Schwartz, J., and Blackstone, C. (2022). ER proteins decipher the tubulin code to regulate organelle distribution. Nature *601*, 132–138.

55. Zhu, K., Yang, C., Xiaotong, S., Zuodong, Y., Yuanzhu, G., Chuang, L., Rui, W., Zhibin, M., Huazhang, Z., Liang, Z., Shengjin, L., Hongmin, Z., et al. (2022). The phosphorylation and dephosphorylation switch of VCP/p97 regulates the architecture of centrosome and spindle. Cell Death Differ. *29*, 2070–2088.

56. Hirota, T., Kunitoku, N., Sasayama, T., Marumoto, T., Zhang, D., Nitta, M., Hatakeyama, K., and Saya, H. (2003). Aurora-A and an interacting activator, the LIM protein Ajuba, are required for mitotic commitment in human cells. Cell *114*, 585–598.

57. Marumoto, T., Hirota, T., Morisaki, T., Kunitoku, N., Zhang, D., Ichikawa, Y., Sasayama, T., Kuninaka, S., Mimori, T., Tamaki, N., et al. (2002). Roles of aurora-A kinase in mitotic entry and G2 checkpoint in mammalian cells. Gene Cell. *7*, 1173–1182.

58. Du, J., and Hannon, G.J. (2004). Suppression of p160ROCK bypasses cell cycle arrest after Aurora-A/STK15 depletion. Proc. Natl. Acad. Sci. USA *101*, 8975–8980.

59. Yang, H., Burke, T., Dempsey, J., Diaz, B., Collins, E., Toth, J., Beckmann, R., and Ye, X. (2005). Mitotic requirement for aurora A kinase is bypassed in the absence of aurora B kinase. FEBS Lett. *579*, 3385–3391.

60. Hoar, K., Chakravarty, A., Rabino, C., Wysong, D., Bowman, D., Roy, N., and Ecsedy, J.A. (2007). MLN8054, a small-molecule inhibitor of Aurora A, causes spindle pole and chromosome congression defects leading to aneuploidy. Mol. Cell Biol. *27*, 4513–4525.

61. Nikonova, A.S., Astsaturov, I., Serebriiskii, I.G., Dunbrack, R.L., Jr., and Golemis, E.A. (2013). Aurora A kinase (AURKA) in normal and pathological cell division. Cell. Mol. Life Sci. *70*, 661–687.

62. Fu, J., Bian, M., Jiang, Q., and Zhang, C. (2007). Roles of Aurora kinases in mitosis and tumorigenesis. Mol. Cancer Res. *5*, 1–10.

63. Katayama, H., Brinkley, W.R., and Sen, S. (2003). The Aurora kinases: role in cell transformation and tumorigenesis. Cancer Metastasis Rev. *22*, 451–464.

64. Perez-Riverol, Y., Csordas, A., Bai, J., Bernal-Llinares, M., Hewapathirana, S., Kundu, D.J., Inuganti, A., Griss, J., Mayer, G., Eisenacher, M., et al. (2019). The PRIDE database and related tools and resources in 2019: improving support for quantification data. Nucleic Acids Res. *47*, D442–D450.

65. Kuczuk, M.H., and Scott, W.J. (1984). Potentiation of acetazolamide induced ectrodactyly in swv and C57bl/6j mice by cadmium sulfate. Teratology *29*, 427–435.

66. Tresse, E., Salomons, F.A., Vesa, J., Bott, L.C., Kimonis, V., Yao, T.P., Dantuma, N.P., and Taylor, J.P. (2010). VCP/p97 is essential for maturation of ubiquitin-containing autophagosomes and this function is impaired by mutations that cause IBMPFD. Autophagy *6*, 217–227.

67. Cox, J., and Mann, M. (2008). MaxQuant enables high peptide identification rates, individualized p.p.b.-range mass accuracies and proteome-wide protein quantification. Nat. Biotechnol. *26*, 1367–1372.

68. Schwanhäusser, B., Busse, D., Li, N., Dittmar, G., Schuchhardt, J., Wolf, J., Chen, W., and Selbach, M. (2011). Global quantification of mammalian gene expression control. Nature *473*, 337–342.

69. Fischer, M., Zilkenat, S., Gerlach, R.G., Wagner, S., and Renard, B.Y. (2014). Pre- and post-processing workflow for affinity purification mass spectrometry data. J. Proteome Res. *13*, 2239–2249.

70. Chen, J., Bardes, E.E., Aronow, B.J., and Jegga, A.G. (2009). ToppGene Suite for gene list enrichment analysis and candidate gene prioritization. Nucleic Acids Res. *37*, W305–W311.

STAR★METHODS

KEY RESOURCES TABLE

REAGENT or RESOURCE	SOURCE	IDENTIFIER
Antibodies		
Rabbit polyclonal anti-EMC3	Sigma Aldrich	Cat#HPA042372 LOT# R39594; RRID:AB_10795609
Rabbit polyclonal anti-EMC3	Invitrogen	Cat#702736; RRID:AB_2725529
Mouse IgG_{2a} anti-EMC3	Santa Cruz	Cat#sc-365903 LOT# L2314; RRID:AB_10842176
Rabbit polyclonal anti-EMC4	Abcam	Cat#ab184544
Rabbit polyclonal anti-EMC4	Abcam	Cat#ab236141
Rabbit polyclonal anti-EMC1	Sigma Aldrich	Cat#HPA048904 LOT# R58867; RRID:AB_2680552
Guinea pig anti-Foxa2	In house, Made against FOXA2 (aa7-86) GST fusion protein	N/A
Mouse IgG_1 anti-Phospho-Histone H3 (Ser10)	Invitrogen	Cat#MA5-15220; RRID:AB_11008586
Mouse IgG_1 anti-BrdU	Santa Cruz	Cat#sc-32323 LOT#A1619; RRID:AB_626766
Rabbit polyclonal anti-Active Caspase 3	R&D systems	Cat#AF835; RRID:AB_2243952
Rabbit polyclonal anti-ATF4	Abcam	Cat#ab184909 LOT#GR321752-7; RRID:AB_2819059
Rabbit polyclonal anti-ATF6	Thermo Fisher Scientific	Cat#PA520215 LOT#TB2528944; RRID:AB_11156621
Rabbit polyclonal anti-BiP	Sigma Aldrich	Cat#G9043; RRID:AB_2279879
Rabbit polyclonal anti-GADD34	Thermo Fisher Scientific	Cat#PA1-139 LOT#QD219449; RRID:AB_2539894
Mouse IgG_1 anti-β actin	Seven Hill Bioreagents	Cat#LMAB-C4; RRID:AB_451715
Rat IgG_{2a} anti-α tubulin	Invitrogen	Cat#MA1-80017 LOT#SH2434205; RRID:AB_2210201
Mouse IgG_{2b} anti-γ tubulin	Santa Cruz	Cat#sc-17788 LOT#H2117; RRID:AB_628418
Mouse IgG_1 anti-Aurora A	Invitrogen	Cat#45–8900 LOT#TI277144; RRID:AB_2533839
Rabbit polyclonal anti-Aurora A	Invitrogen	Cat#PA5-34700 LOT#UJ2866088C; RRID:AB_2552052
Rabbit polyclonal anti-Phospho-Aurora A (Thr288)	Invitrogen	Cat#44–1210G LOT#RG241362; RRID:AB_1461184
Rabbit polyclonal anti-Phospho-Aurora A (Thr288)/Aurora B (Thr232)/Aurora C (Thr198)	Cell signaling	Cat#2914S LOT#9; RRID:AB_2061631
Rabbit polyclonal anti-TPX2	Novus	Cat#NB500-179 LOT#D-2; RRID:AB_10002747
Rabbit polyclonal anti-VCP	GeneTex	Cat#GTX101089 LOT#39834; RRID:AB_1952544
Rabbit polyclonal anti-Myc	Cell signaling	Cat#2278s LOT#5; RRID:AB_490778
Rabbit polyclonal anti-Flag	Sigma Aldrich	Cat#F7425 LOT#078M4886V; RRID:AB_439687

(*Continued on next page*)

Continued

REAGENT or RESOURCE	SOURCE	IDENTIFIER
Rabbit polyclonal anti-GAPDH	BETHYL	Cat#A300-641A; RRID:AB_513619
Mouse IgG_1 anti-Lamin A/C	Santa Cruz	Cat#sc-376248 LOT# E1019; RRID:AB_10991536
Mouse IgG2a anti-Centrin	Millipore	Cat#04–1624 LOT#2829820; RRID:AB_10563501
Chemicals, peptides, and recombinant proteins		
Puromycin Dihydrochloride	Sigma Aldrich	Cat#P8833
thymidine	Sigma Aldrich	Cat#T1895
nocodazole	Sigma Aldrich	Cat#SML1665
RO3306	Sigma Aldrich	Cat# 217721
Annexin V, Alexa Fluor™ 647 conjugate	Invitrogen	Cat#A23204
FxCycle™ PI/RNase Staining Solution	Thermo Fisher Scientific	Cat# F10797
Critical commercial assays		
ApopTag® Peroxidase *In Situ* Apoptosis Detection Kit	Sigma Aldrich	Cat#S7100
NE-PER Nuclear and Cytoplasmic Extraction Reagents	Thermo Fisher Scientific	Cat#78833
Lipofectamine RNAiMAX Transfection Reagent	Invitrogen	Cat#13778150
X-tremeGENE™ HP DNA Transfection Reagent	Sigma Aldrich	Cat#XTGHP-RO
Click-iT™ Plus EdU Alexa Fluor™ 647 Flow Cytometry Assay Kit	Thermo Fisher Scientific	Cat# C10634
SYTOX™ AADvanced™ Dead Cell Stain Kit	Invitrogen	Cat# S10274
RNeasy Micro Kit	Qiagen	Cat# 74004
iScript cDNA synthesis kit	Bio-Rad	Cat# 1708891
Dynabeads Co-Immunoprecipitation Kit	Invitrogen	Cat# 14321D
µMACS DYKDDDDK Isolation Kit	Miltenyi Biotec	Cat# 130-101-591
µMACS c-myc Isolation Kit	Miltenyi Biotec	Cat# 130-091-123
Deposited data		
Mass spectrometry proteomics data on Myc-Emc3 co-immunoprecipitates	ProteomeXchange Consortium via the PRIDE (Perez-Riverol et al.[64]) partner repository	PXD017773
Experimental models: Cell lines		
NIH3T3	ATCC	Cat# CRL-1658; RRID:CVCL_0594
HeLa	ATCC	Cat# CRM-CCL-2; RRID:CVCL_0030
Experimental models: Organisms/strains		
Emc3^{fl} mice	previous work by this group (Tang et al.[15])	N/A
Dermo1-Cre	Jackson Labs	stock # 008712
CAG-CAT-EGFP	Jackson Labs	stock # 024636
Oligonucleotides		
control siRNA	Thermo Fisher Scientific	Cat# 4457289
Emc3 siRNA 1	Thermo Fisher Scientific	Cat# s82552
Emc3 siRNA 2	Thermo Fisher Scientific	Cat# s82553
Emc4 siRNA 1	Thermo Fisher Scientific	Cat# s86111
Emc4 siRNA 2	Thermo Fisher Scientific	Cat# s86112
VCP siRNA 1	Thermo Fisher Scientific	Cat# s114337
VCP siRNA 2	Thermo Fisher Scientific	Cat# s114338
non-target control shRNA	Sigma Aldrich	Cat#SHC016
human Emc3 shRNA	Sigma Aldrich, MISSION shRNA	Cat#TRCN0000136654

(*Continued on next page*)

Continued

REAGENT or RESOURCE	SOURCE	IDENTIFIER
Mouse *Emc3* Taqman probe	Thermo Fisher Scientific	AssayID Mm01184718_g1
spliced form of XBP1 TapMan probe	Thermo Fisher Scientific	AssayID Mm03464496_m1
unspliced XBP1 TapMan probe	Thermo Fisher Scientific	AssayID Mm03464497_s1
18S TaqMan probe	Applied Biosystems	Cat# 4352930E
Recombinant DNA		
pShuttle Myc-Emc3	previous work by this group (Tang et al.[15])	N/A
pCMV6 Aurora A-Flag	this paper	N/A
VCP-EGFP	Nico Dantuma (Tresse et al.[66])	Addgene # 23971
Software and algorithms		
intensity-based absolute quantification (iBAQ) method	Schwanhäusser et al.[68]	N/A
R based AP-MS analyses package *apmsWAPP*	Fischer et al.[69]	N/A
Toppgene's Toppfun	Chen et al.[70]	N/A

RESOURCE AVAILABILITY

Lead contact

Further information and requests for reagents may be directed to, and will be fulfilled by, the lead contact, jeffrey.whitsett (jeffrey.whitsett@cchmc.org).

Materials availability

All unique/stable reagents generated in this study are available from the lead contact with a completed Materials Transfer Agreement.

Data and code availability

The mass spectrometry proteomics data have been deposited to the ProteomeXchange Consortium via the PRIDE[64] partner repository with the dataset identifier PXD017773; the R code used for AP-MS analyses package *apmsWAPP* is attached as supplement. Any additional information required to reanalyze the data reported in this paper is available from the lead contact upon request.

EXPERIMENTAL MODEL AND SUBJECT DETAILS

Mice

Mice were housed in pathogen-free conditions according to the protocols approved by the Institutional Animal Care and Use Committee at Cincinnati Children's Hospital Research Foundation. Conditional *Emc3*^{fl} mice were generated as described.[15] For mesenchyme-specific deletion of *Emc3*, *Emc3*$^{fl/fl}$ mice were bred with *Dermo1-Cre*[27](Jackson Labs, stock number 008712). To label and track Cre-mediated recombination, *CAG-CAT-EGFP* (Jackson Labs, stock number 024636) mice were used to generate *CAG-CAT-EGFP*[31]; *Emc3*$^{fl/fl}$ mice and bred with *Dermo1-Cre*; *Emc3*$^{fl/+}$ mice. 2–4 month- females and 2–6 month-males were used for breeding. For fetal studies, mice were mated overnight, and the presence of a vaginal plug was defined as E0.5. Both male and female embryos were collected and examined. No discrepancy of phenotypes was observed between genders.

Cell lines

NIH3T3 and HeLa cells were obtained from ATCC and cultured in Dulbecco's Modified Eagle's Medium (DMEM) with 10% fetal bovine serum and 1% penicillin/streptomycin solution.

MEF cells

MEFs were isolated from E13.5 embryos and cultured in culture media containing Dulbecco's Modified Eagle's Medium (DMEM) with 10% fetal bovine serum, 1% L-glutamine and 1% penicillin/streptomycin

solution. For each embryo, cut off the head above the eyes and tear out the heart and liver. Place the rest of the embryo in a covered Petri dish with 10mL 0.25% trypsin-EDTA. Chop up and then mince the tissue into pieces before place the dish in the 37°C tissue culture incubator. Incubate for 30 min while pipetting up and down several times every 10 min. Add 20 mL culture media to inactivate trypsin. Let the cell suspensions sit for 10 min and transfer the supernatant of cell suspension to a 10cm culture plate. The following morning, remove old culture medium and replace with fresh medium. Split the cells when they reach confluency. This is passage number 1.

METHOD DETAILS

Alizarin red and alcian blue staining of bone and cartilage

Cartilage and bone staining was performed essentially as described by Kuzuk and Scott.[65] E18.5 fetuses were submerged in hot water for approximately 30 seconds and the skin was peeled away prior to fixation in 95% ETOH for at least 5 days. Fetuses were eviscerated and the tongues removed prior to staining in Alcian blue solution (0.075g Alcian blue/100 mL glacial acetic acid/400mL 95% ETOH) overnight. Fetuses were rinsed in 95% ETOH twice for 1 hour each prior to maceration in 2% KOH for several hours until the muscle appears slightly opaque. Once partially cleared, fetuses were stained in Alizarin red S (50 mg Alizarin red S/1 liter of 2% KOH) 1 hour to overnight, and then subjected to additional clearing in graded concentrations 80%/20%, 60%/40%, 40%/60% and 20%/80% of 2% KOH/glycerin. All KOH solutions were made using tap water.

Lung histology, immunohistochemistry and immunofluorescence

Lungs from E16.5 and E18.5 embryos were fixed in 4% paraformaldehyde, embedded in paraffin or OCT compound and sectioned at 5 or 7μm respectively. Histological staining and immunohistochemistry were performed on paraffin sections according to standard protocols. TUNEL staining was performed on paraffin sections using ApopTag® Peroxidase *In Situ* Apoptosis Detection Kit (Sigma Aldrich). Bright-field images were obtained using a Zeiss Axio ImagerA2 microscope equipped with AxioVision Software. Immunofluorescence staining was performed on E16.5 lung cryosections and fluorescence images were obtained using a Nikon A1Rsi inverted laser confocal microscope.

Constructs, siRNAs and shRNAs

The Myc-Emc3 construct was made as described.[15] The C-terminal Myc-DDK–tagged Aurora A construct was purchased from ORIGENE (CAT#: MR229680). To make single Flag-tagged Aurora A, Aurora A cDNA was amplified by PCR using primers F (ACTGGATCCGGTACCGAGGAG) and R (TTCTCGAGTTACTTGTCAT CATCGTCCTTATAGTCAGATGATTTGCTGGTTGGCTCTTTGC) and then subcloned into the pCMV6 vector using KpnI and XhoI restriction sites. The C-terminal EGFP-tagged VCP construct[66] was a gift from Nico Dantuma (Addgene plasmid # 23971; http://n2t.net/addgene:23971; RRID:Addgene_23971).

The following Silencer Select siRNAs (Thermo Fisher Scientific) were used for transfection: control siRNA (Cat.# 4457289), *Emc3* siRNA 1 (Cat.#s82552), *Emc3* siRNA 2 (Cat.#s82553), *Emc4* siRNA 1 (Cat.#s86111), *Emc4* siRNA 2 (Cat.#s86112), *VCP* siRNA 1 (Cat.#s114337), and *VCP* siRNA 2 (Cat.#s114338).

The following shRNAs were used for infection in HeLa cells: non-target control shRNA (SHC016, Sigma Aldrich), human Emc3 shRNA (MISSION shRNA, TRCN0000136654, Sigma Aldrich).

Cell transfection and western blots

Cell transfection with siRNA was done using Lipofectamine RNAiMAX Transfection Reagent (Invitrogen) following the manufacturer's protocol. Cell transfection with plasmids was done using X-tremeGENE™ HP DNA Transfection Reagent (Sigma Aldrich). Nuclear and cytoplasmic fractionation was done using NE-PER Nuclear and Cytoplasmic Extraction Reagents (Thermo Fisher Scientific) following the manufacturer's protocol. HeLa cell infection with lentiviral shRNA was done with the presence of 8 μg/mL polybrene and 24 hours after infection, cells were cultured in full media with 2 μg/mL Puromycin Dihydrochloride (P8833, Sigma Aldrich) for 3 days to enrich infected cells. Cells were cultured in Puromycin Dihydrochloride free media for 2 days before any analysis.

Upon harvest, cells were lysed in lysis buffer (50 mM Tris-HCl, pH 7.4, 150 mM NaCl, 1 mM EDTA, and 1% Triton X-100 supplemented with Proteinase Inhibitor Cocktail). For co-immunoprecipitation (co-IP) assays with transfected cells, cells were harvested ~36 hours after transfection. Co-IP assays by c-Myc antibody

and Flag antibody were done using μMACS c-myc Isolation Kit and μMACS DYKDDDDK Isolation Kit (Miltenyi Biotec) respectively following the manufacturer's protocol. Co-IP with endogenous proteins in HeLa cells was done using Dynabeads Co-Immunoprecipitation Kit (Invitrogen) following the manufacturer's protocol. Briefly, 10μg EMC4 antibody (rabbit polyclonal antibody, Abcam, Cat.# ab236141) or Aurora A antibody (rabbit polyclonal antibody, Invitrogen, Cat.# PA5-34700) or Rabbit IgG were coupled to 1.5mg Dynabeads M−270 Epoxy. After extensive washing, the antibody-coupled beads were incubated overnight with the cell lysates of ~50mg human HeLa cells synchronized in mitosis. After extensive wash on a magnet, the precipitates were eluted from the Dynabeads and were subsequently analyzed by Western blot.

Proteins were resolved by SDS-PAGE using 4%–12% gels (NuPAGE Novex gel, Invitrogen) and the MES SDS running buffer (NuPAGE, Invitrogen). Chemiluminescence was observed using the Luminata Western HRP substrate (Millipore) and images were generated using the ChemiDoc Touch imaging system (Bio-Rad) and quantified using Image Lab software (Bio-Rad). At least 3 independent experiments were performed, and representative results are shown for each.

Time-lapse imaging

Time-lapse images were acquired using a Nikon Ti-E SpectraX Widefield Microscope with a heated chamber and 5% CO_2. Images were captured at 2-minute intervals using a 20X Plan Apo lens.

Cell synchronization

To arrest cells in S phase, double thymidine block was used: NIH3T3 cells, MEF cells or HeLa cells were incubated with 2.5mM thymidine for 16 hours, released in fresh DMEM (10% FBS) medium for 8 hours, and then blocked again for 16 hours with 2.5 mM thymidine. To obtain M-phase arrested cells, following release from the double thymidine block, cells were treated with DMEM (10% FBS) medium with 100 ng/mL nocodazole for 16 hours. Following release from the nocodazole block, the M-phase cells were harvested by shaking off. To synchronize cells at G2/S for time-lapse imaging, following release from the double thymidine block, NIH3T3 cells or MEF cells were incubated in DMEM (10% FBS) medium with 10μM RO3306 (InSolution Cdk1 Inhibitor IV, Millipore). Cells were carefully and extensively washed 16 hours later and immediately imaged following release into Phenol Red-free DMEM with 10% FBS.

RNA isolation and qPCR

Total RNA was isolated from MEF cells at different passages using a RNeasy Micro Kit (Qiagen). Reverse transcription reactions were performed using an iScript cDNA synthesis kit (Bio-Rad) following the manufacturers' instructions. Quantitative PCR (qPCR) was performed using a StepOnePlus Real-Time PCR System and TaqMan gene expression assays (Applied Biosystems). *Emc3* RNA (Taqman probe Mm01184718_g1) was normalized to the levels of 18S RNA (TaqMan probe 4352930). The levels of the spliced form of XBP1 (TapMan probe Mm03464496_m1) was normalized to that of the unspliced XBP1 (TapMan probe Mm03464497_s1). Data are mean ± SEM, with 2-tailed Student's t-test. Statistical analyses were performed in GraphPad Prism 8 (GraphPad Software, Inc.).

Flow cytometry

Cultured cells were trypsinized into single cell suspensions. DNA content was examined by PI staining (FxCycle™ PI/RNase Staining Solution, Cat.# F10797, Thermo Fisher Scientific). DNA replication was examined by Click-iT™ Plus EdU Alexa Fluor™ 647 Flow Cytometry Assay Kit (Thermo Fisher Scientific, Cat.#C10634). To quantify apoptosis, cultured cells were lightly trypsinized into single cell suspensions and were allowed to recover from membrane disruption for 30–45 minutes in the incubator. After that, the cells were stained by Annexin V, Alexa Fluor™ 647 conjugate (Invitrogen, Cat.# A23204) and SYTOX™ AADvanced™ Dead Cell Stain Kit (Invitrogen, Cat.#S10274) according to the manufacturer's protocol. As soon as the staining was done, the cells were analyzed by flow cytometry and the ratio of Annexin V positive cells to total live cells was quantified. Flow cytometry was performed on a BD LSR Fortessa and data analyzed with FlowJo 10.0.8 software.

Proteomic analysis

Mass spectrometry of control and EMC3 co-immunoprecipitates was done at Pacific Northwest National Laboratory. Co-purified proteins were dissolved in 20 μL 50 mM NH_4HCO_3 containing 8 M urea and 5 mM dithiothreitol and incubated for 15 min at 37 ºC with shaking at 800 rpm. The free thiol groups

were alkylated by adding 400 mM iodoacetamide to a final concentration of 10 mM and incubated for 30 min under the same conditions. Samples were diluted 8 folds with 50 mM NH_4HCO_3, and 1 M $CaCl_2$ was added to a final concentration of 1 mM. The digestion was carried out overnight at 37 ºC using trypsin at 0.1 μg trypsin per sample. Digested peptides were desalted using C18 spin columns (Ultramicrospin columns, C18, 3–30 μg capacity, Nest Group) and dried in a vacuum centrifuge.

Peptides were analyzed by liquid chromatography-tandem mass spectrometry on a Waters NanoAquity UPLC system with a custom packed C18 column (70 cm × 75 μm i.d., Phenomenex Jupiter, 3 μm particle size, 300 Å pore size) coupled with an Orbitrap Fusion Lumos mass spectrometer (Thermo Fisher Scientific). Elution was carried out using the following gradient of water (solvent A) and acetonitrile (solvent B) both containing 0.1% formic acid: 1–8% B for 2 min, 8–12% B for 18 min, 12–30% B for 55 min, 30–45% B for 22 min, 45–95% B for 3 min, hold for 5 min in 95% B and 99–100% B for 10 min. Eluting peptides were analyzed online by nanoelectrospray ionization and MS1 scans were collected over 300–1800 *m/z* at a resolution of 60,000 at 400 *m/z*. The MS2 scans were collected in data-dependent acquisition with 2 second cycles and high-energy collision induced dissociation (HCD) fragmentation (2.0 *m/z* isolation width; 30% normalized collision energy; 7,500 resolution at 400 *m/z*), before being dynamically excluded for 30 s. Data were searched with MaxQuant software (v.1.5.5.1)[67] against the mouse reference proteome database from Uniprot Knowledge Base (downloaded August 14, 2018). Peptides were required to be cleaved by trypsin in both termini, but 2 undigested sites were allowed per peptide. The following variable modifications were considered: on acetylation and oxidation on protein N-terminal and methionine, respectively. Carbamidomethylation of cysteine residues was set as a fixed modification. Mass shift tolerance was used as the default setting of the software.

QUANTIFICATION AND STATISTICAL ANALYSIS

Statistical analysis

Statistical analysis was done on Prism 8. Values are expressed as the mean ± SEM. Details for specific analysis are described in the figure legends.

Quantification of cell proliferation and cell death in the lung

Cell proliferation in E16.5 lung cryosections was characterized by BrdU and phospho histone H3 immunofluorescence and quantified in Nikon Elements General Analysis 4.50. For BrdU labeling, E16.5 pregnant mice were injected intraperitoneally with BrdU at 50 mg/kg of body weight and the animals were sacrificed 2 hours after the injection. For quantification of immunofluorescence staining, tile scans of the whole lung were taken on a Nikon A1Rsi inverted laser confocal microscope; approximately 10, 40× random regions were selected. In each image, an average of 1,000 cells was counted for analysis. A total of 10,000–15,000 cells were counted per mouse. A 2-tailed Student's t-test was used to determine statistical differences between genotypes. Cell death in E16.5 paraffin sections were characterized by TUNEL assay and Caspase-3 immunohistochemistry and quantified in Nikon Elements General Analysis RGB 4.50. Widefield tile scans were taken of the whole lung on a Nikon Eclipse Ni-E upright microscope; 10–15, 20X random alveolar regions were selected. In each image, an average of 2,000 cells was counted for analysis. A total of 20,000–30,000 cells were counted per mouse. A 2-tailed Student's t-test was used to determine statistical differences between genotypes.

Quantification of mass spectrometry data

Mass spectrometry data was performed using the intensity-based absolute quantification (iBAQ) method by MaxQuant software.[68] Missing values were imputed with half the minimum value of the lowest iBAQ score in the quantification data matrix. To identify potential EMC3 protein-protein interaction (PPI) partners, we utilized the R based AP-MS analyses package *apmsWAPP* and specifically the sub package TSPM which utilizes a two-stage-Poisson model to determine significant protein-protein interactions.[69] Spectral counts were normalized using the "DESeq" designation and proteins were filtered using "overallVar" with a var.cutoff = 0.1. Proteins with a p value<.05 were deemed potential EMC3 partners and were visualized in a zscore normalized heatmap of the TSPM normalized spectral counts. Functional enrichment analyses of potential EMC3 PPI partners were determined using Toppgene's Toppfun[70] (https://toppgene.cchmc.org). Significant hits poignant to this project were represented in a bar graph of the $-\log_{10}$(pvalue).